Geophysical Journal International

Geophys. J. Int. (2023) **234,** 1943–1964
Advance Access publication 2023 April 26
GJI Seismology

https://doi.org/10.1093/gji/ggad178

Temporal variations of the ambient seismic field at the Sardinia candidate site of the Einstein Telescope

M. Di Giovanni,[1,2] S. Koley,[1,2] J. X. Ensing,[3] T. Andric,[1,2] J. Harms,[1,2] D. D'Urso,[4,5] L. Naticchioni,[6,7] R. De Rosa,[8,9] C. Giunchi,[10] A. Allocca,[8,9] M. Cadoni,[11,12] E. Calloni,[8,9] A. Cardini,[12] M. Carpinelli,[4,5,12] A. Contu,[12,13] L. Errico,[8,9] V. Mangano,[6,7] M. Olivieri,[14] M. Punturo,[15] P. Rapagnani,[6,7] F. Ricci,[6,7] D. Rozza,[4,5] G. Saccorotti,[10] L. Trozzo,[9] D. Dell'aquila,[4,5] L. Pesenti,[4,5] V. Sipala[4,5] and I. Tosta e Melo[4,5]

[1] *Gran Sasso Science Institute (GSSI), I-67100 L'Aquila, Italy. E-mail: soumen.koley@gssi.it*
[2] *INFN, Laboratori Nazionali del Gran Sasso, I-67100 Assergi (AQ), Italy*
[3] *AstroCeNT, Nicolaus Copernicus Astronomical Center of the Polish Acedemy of Sciences, PL-00716 Warsaw, Poland*
[4] *Department of Chemistry and Pharmacy, Universit'a degli Studi di Sassari, I-07100 Sassari, Italy*
[5] *INFN, Laboratori Nazionali del Sud, I-95125 Catania, Italy*
[6] *Department of Physics, Sapienza Università di Roma, I-00185 Roma, Italy*
[7] *INFN, sezione di Roma 1, I-00185 Roma, Italy*
[8] *Department of Physics, Universit'a degli Studi di Napoli Federico II, I-80126 Napoli, Italy*
[9] *INFN, sezione di Napoli, I-80126 Napoli, Italy*
[10] *Istituto Nazionale di Geofisica e Vulcanologia, sezione di Pisa, I-56123 Pisa, Italy*
[11] *Department of Physics, Università degli Studi di Cagliari, I-09123 Cagliari, Italy*
[12] *INFN, sezione di Cagliari, I-09042 Monserrato (CA), Italy*
[13] *INAF—Osservatorio Astronomico di Cagliari, I-09042 Cagliari, Italy*
[14] *Istituto Nazionale di Geofisica e Vulcanologia, sezione di Bologna, I-40100 Bologna, Italy*
[15] *INFN, sezione di Perugia, I-06123 Roma, Italy*

Accepted 2023 April 20. Received 2023 April 11; in original form 2022 November 7

SUMMARY

Einstein Telescope (ET) is a proposed underground infrastructure in Europe to host future generations of gravitational-wave (GW) detectors. One of its design goals is to extend the observation band of terrestrial GW detectors from currently about 20 Hz down to 3 Hz. The coupling of a detector to its environment becomes stronger at lower frequencies, which makes it important to carefully analyse environmental disturbances at ET candidate sites. Seismic disturbances pose the greatest challenge since there are several important mechanisms for seismic vibrations to produce noise in ET, for example, through gravitational coupling, stray light, or through harmful constraints on the design of ET's control system. In this paper, we present an analysis of the time-variant properties of the seismic field at the Sardinia candidate site of ET connected to anthropogenic as well as natural phenomena. We find that temporal variations of source distributions and of the noise spectra generally follow predictable trends in the form of diurnal, weekly, or seasonal cycles. Specific seismic sources were identified such as road bridges, which produce observable disturbances underground. This information can be used to adapt a detector's seismic isolation and control system.

Key words: Time-series analysis; Seismic instruments; Seismic noise; Einstein Telescope; Gravitational waves.

1 INTRODUCTION

During the last few years, we have witnessed a real revolution in physics and astronomy thanks to the first detections of gravitational waves (GWs) from mergers of compact objects like black holes and neutron stars (LIGO and Virgo Collaboration 2019; LVK Collaboration 2021a, b). GWs are *ripples* in space–time generated by some of the most energetic processes in the Universe. Albert Einstein predicted the existence of GWs in 1916 in his general theory of relativity (Einstein 1916), where he showed that massive accelerating objects (such as the aforementioned neutron stars or black holes orbiting around each other) would disrupt space–time in such a way that waves of undulating space–time would propagate at the speed of light in all directions away from the source, carrying information about their sources as well as clues to the nature of gravity itself (Einstein 1916). The strongest GWs are produced by catastrophic events such as colliding black holes, supernovae (massive stars exploding at the end of their lifetimes) and colliding neutron stars (Schutz 1989, 1996; Baiotti 2020; Abdikamalov *et al.* 2020; Barausse & Lapi 2020; Bailes *et al.* 2021). Other waves are predicted to be caused by the rotation of neutron stars that are not perfect spheres (Haskell & Schwenzer 2020) and possibly even the remnants of gravitational radiation created by the Big Bang (Caprini & Figueroa 2020)

The first attempts to detect GWs date back to the 1960s when normal-mode observations of Earth were used to set upper limits on the amplitude of GWs (Forward *et al.* 1961). Joe Weber, who was part of this team, went on to build the first prototype of a resonant-bar detector (Weber 1967), that is, an aluminum cylinder that would resonate at the passage of a GW. Resonant bars were the main type of detectors for the search of GWs up to the end of the 1990s, but their sensitivities were not enough to detect a GW event. Since then, the GW community has shifted to L-shaped Michelson interferometers (Fig. 1) with arms composed of optical resonators designed to observe GWs in a frequency band between 20 Hz and a few kHz (Dooley *et al.* 2020). In this way, the passage of a GW produces interference between the laser beams travelling in the interferometer. With an arm length of a few kilometres, they can achieve a strain sensitivity of about $2 \times 10^{-23}\,\mathrm{Hz}^{-1/2}$ around 100 Hz for binary black holes/binary neutron star mergers. Currently, there are four operational detectors: Advanced Virgo (AdVirgo), located in Italy (Virgo Collaboration 2014); Advanced LIGO Hanford and Livingston (aLIGO), located in the United States (LIGO Scientific Collaboration 2015) and KAGRA in Japan (KAGRA Collaboration 2019). Moreover, the constant upgrades to current generation GW detectors and their much improved sensitivities made the detection of GW events a common occurrence. The first observation of a binary neutron-star merger also proved the feasibility of joint GW and electromagnetic observations, thus opening the era of multimessenger astronomy (LIGO and Virgo Collaboration 2017a, b).

The sensitivity to the extremely small strain signals produced by GWs makes the detectors sensitive to ground motion induced by seismic noise (Fiori *et al.* 2020a). If seismic disturbances are strong enough, they can cause interruptions of the detector operation as well (Effler *et al.* 2015; Coughlin *et al.* 2017; Mukund *et al.* 2019a, b). To mitigate the effects of seismic noise, active (e.g. ground tilt controls for the mirrors) and passive (inverted pendulums as suspensions for the mirrors) seismic insulators have been installed in GW detectors. For future generation detectors like the Einstein Telescope (ET), even more efficient seismic-attenuation systems, currently under development, are foreseen. The discussion of such control systems is beyond the scope of this paper, but can be found in, for example, Braccini *et al.* (2000), Beker *et al.* (2012b), Acernese *et al.* (2014), Ward *et al.* (2020) and ET Science Team (2020). Nevertheless, the detection capability of GWs can still be reduced by seismic noise (Fiori *et al.* 2020a).

Pioneering studies by Gutenberg (1958) and later by Frantti (1963) were the first to classify seismic noise sources into different categories. Two broad categories were introduced: natural (Longuet-Higgins 1950; Ward & Crawford 1966; Cessaro 1994; Withers *et al.* 1996; Acernese *et al.* 2004; Coward *et al.* 2005; Virgo Collaboration 2006; Burtin *et al.* 2008; Anthony *et al.* 2018; Smith & Tape 2019; Dybing *et al.* 2019; Virgo Collaboration 2022; Anthony *et al.* 2022) and anthropogenic (Acernese *et al.* 2004; Virgo Collaboration 2006; Saccorotti *et al.* 2011; Piccinini *et al.* 2020; Poli *et al.* 2020; Virgo Collaboration 2022). Several other studies that support this classification have been extensively discussed by Bonnefoy-Claudet *et al.* (2006). Seismic noise in the frequency band 0.05–1 Hz is typically marine in origin, that is, noise generated by microseisms from sea waves (Longuet-Higgins 1950; Cessaro 1994; Chevrot *et al.* 2006; Koper & Burlacu 2015; Anthony *et al.* 2022). Above a few Hertz, anthropogenic noise can dominate especially in the vicinity of roads, bridges and railway tracks. Studies by Seo (1997) showed that this transition is also dependent on the local geology at the site. Under similar noise illumination conditions, a soft-soil site is expected to transition to the anthropogenic band at a lower frequency compared to a hard-rock site.

These seismic disturbances can affect GW data in many ways (Virgo Collaboration 2004, 2006, 2011b, a; Koley 2020; Fiori *et al.* 2020a; Virgo Collaboration 2022). They can cause noise in the detector's observation band, for example, through up-conversion of oceanic microseisms created by stray light scattered back from seismically excited surfaces into the main beam of the interferometer (Accadia *et al.* 2010), or as residual seismic disturbances passing through the seismic-isolation system. Seismic disturbances at frequencies below a few Hertz can hinder the control of the detector and ultimately lead to control noise in the observation band (Martynov *et al.* 2016). Furthermore, mass–density fluctuations can interact directly with the mirrors through gravitational forces leading to so-called Newtonian noise (NN, Saulson 1984; Beccaria *et al.* 1998; Harms 2019). For this reason, seismic characterization studies at the candidate sites to host GW detectors are paramount together with detailed modelling of the seismic fields (Beker *et al.* 2015; Amann *et al.* 2020; Koley *et al.* 2022; Harms *et al.* 2022). For example, source locations of oceanic microseisms are expected to show a distribution characteristic for the seasons leading to a seasonal variation in directions of the seismic waves and in the amplitude of seismic noise (Stutzmann *et al.* 2009). This understanding can potentially be exploited for the design of active seismic isolation systems. Since, at other sites of GW interferometers, anthropogenic sources of seismic waves were identified out to distances $\simeq 10$ km (Saccorotti *et al.* 2011), studies of the variations of anthropogenic noise with distance will provide a first indication of the radius of the region around the ET vertices where human activities should be controlled. Moreover, significant temporal variations in the NN band, including diurnal and weekly cycles, has implications for NN cancellation, for which the filters will have to be adaptive or updated regularly to follow these variations.

The GW community has been planning the construction of a next-generation GW detector called ET, since 2010 (Punturo *et al.* 2010; ET Science Team 2010, 2011, 2020). The improvements of ET with respect to current-generation detectors include the extension of the observation band to lower frequencies, that is, from the current limit of about 20–3 Hz, and an improvement of the sensitivity by about a factor 10 across the band covered by current detectors (ET Science Team 2020). Furthermore, ET will be composed of three pairs of nested interferometers arranged in an equilateral triangle (also called xylophone configuration) with the sides 10 km long and hosted at a depth currently planned between 200 and 300 m to reduce seismic motion at the input of the suspension system of the mirrors, and to reduce the impact of atmospheric disturbances (Hutt *et al.* 2017). For each interferometer pair, one interferometer will be optimized for low frequencies ($3\,\mathrm{Hz} < f < 40\,\mathrm{Hz}$) and the other for high frequencies ($f > 40$ Hz, ET Science Team 2020).

As a consequence of the extension of the bandwidth to 3 Hz and the sharp increase in sensitivity, a careful assessment of seismic

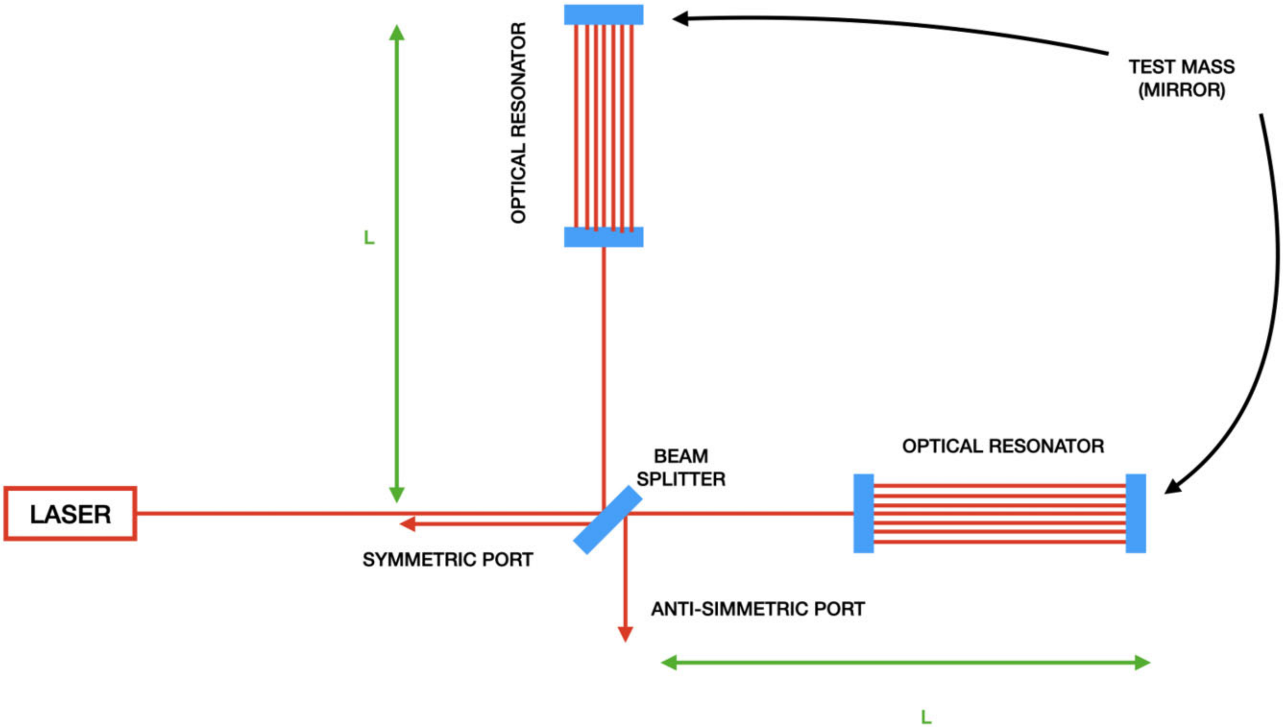

Figure 1. A basic Michelson interferometer with arm lengths *L*. Either output port can be used to obtain the GW signal. A design convention is to use the antisymmetric port. The principle behind the use of a Michelson interferometer is that even a small length difference in the arms of the detector will cause interference between the light beams travelling in it and recombined at the output by the beam splitter. Therefore, a GW passing through the arms of the interferometer will deform the geometry of space-time causing a small difference in the length of the arms of the detector. This difference is of the order of 10^{-18} m. The optical configuration used in current generation of GW interferometers is an extension of the basic Michelson interferometer. The most relevant additional feature is that of optical resonant cavities in the arms of the detector. On resonance with the incoming light, the light field inside the cavity is resonantly enhanced by multiple reflections. This resonant enhancement is typically used to increase the precision on an interferometric phase measurement.

noise at the candidate sites for ET is necessary to guarantee a suitable environment for this future detector (Amann *et al.* 2020). Therefore, the scope of this work is to provide a characterization of seasonal and ambient-noise variations at the Sardinia candidate site for ET and to extend the studies of previous papers (Naticchioni *et al.* 2014, 2020; Di Giovanni *et al.* 2021).

The paper is organized in the following way. In Section 2, we give a recap of the general properties of the Sardinia candidate site; Section 3 is devoted to an overview of the instrument set up used to acquire the data; Section 4 covers the seasonal noise variations caused by sea-wave noise; Section 5 shows evidence of the transition between microseismic and anthropogenic noise; the effects of wind on seismic data are shown in Section 6; in Section 7, we discuss the seismic noise variations in the anthropogenic band and some of the noise sources identified in the vicinity of the site.

2 THE SITE

As already outlined in previous studies (Naticchioni *et al.* 2014, 2020; Di Giovanni *et al.* 2021), the area around the former Sos Enattos mine in Sardinia (Italy) was selected as one of the candidate sites to host ET (ET Science Team 2011, 2020) for the very low seismic rate of Sardinia (ET Science Team 2011), with no events over $M_\mathrm{L} = 2.5$ (local magnitude) recorded within 50 km from the mine since 1980 when systematic recording of earthquakes started (Di Giovanni *et al.* 2021). These observations are in agreement with the geodynamic evolution of the Corsica–Sardinia microblock (Carmignani *et al.* 2004; Faccenna *et al.* 2014; Magrini *et al.* 2020), which, after completing the clockwise rotation due to the opening of the Liguro–Provencal basin roughly between 30 and 15 Ma (mega annum), remained unaffected by the fast extension, leading to the formation of the Tyrrhenian Sea in the last 15 Ma. This is also confirmed by the present-day deformation, showing very little motion of the Corsica–Sardinia microblock with respect to the Eurasian plate (Faccenna *et al.* 2014). Sos Enattos was also selected because the mine provides the appropriate infrastructure to support characterization studies underground, at the depths foreseen for the construction of ET (ET Science Team 2011). Moreover, the mine lays on a crystalline basement of mica schist, quartzite, orthogneiss and granitoid rocks, that is known to provide a stable environment for the construction of large underground facilities (Beker *et al.* 2012a; Naticchioni *et al.* 2020). If the Sardinia site is selected, one of the three vertices of ET would lie close to Sos Enattos, but the exact location of the vertices and the orientation of the interferometer is still to be decided. Site characterization studies have focused on the area around the mine, and only recently the characterization of the other two corner areas have started.

The mine is located 30 km northeast of the city of Nuoro and includes tunnels for a total length of about 50 km excavated in about 2000 yr of mining exploitation to harvest zinc and lead. Nevertheless, these tunnels will not be used for the construction of ET, for which a completely new infrastructure will be built. Nowadays, the mine is dismissed but is considered a regional heritage site, therefore it is still manned for environmental safety and guided tours, and occasionally it is used as a quarry. Since 2018, the site also hosts the SarGrav surface laboratory, a facility to conduct experiments in low seismic noise background environments and to provide research and development for future ET technologies (Naticchioni *et al.* 2018).

Through the only tunnel that is still safely accessible, it is possible to reach a depth of about 160 m. Furthermore, the area around Sos Enattos is scarcely inhabited, with a population density of about 13 km^{-2} within 10 km from the site (Eurostat 2019) and there are no major railways, large industrial, or agricultural facilities located within tens of kilometres of the site. These features contribute to make Sos Enattos seismically extremely quiet and suitable to host ET (Di Giovanni *et al.* 2021). In fact, we expect that anthropogenic noise at Sos Enattos is limited to very local activities which, to our knowledge, only include mine maintenance (vehicles driving at the site, lorries unloading their cargo, active water pumps, miners inspecting the site and minor maintenance interventions in the tunnels) and, possibly, farming activities in the nearby fields and pastures. All these activities can be controlled and would be interrupted when ET will become operational.

3 INSTRUMENT SET UP

As of 2022, there are three active permanent seismic stations located at different depths in Sos Enattos, named SOE0 (surface), SOE1 (−84 m) and SOE2 (−111 m) respectively (Fig. 2). The latter has also been part of the Italian seismological monitoring network (INGV Seismological Data Center 2006) as IV.SENA from 2019 to 2021 and is now included in the Mediterranean Very Broadband Seismographic Network (MedNet Project Partner Institutions 1990) as MN.SENA. The scope of the three seismic stations is to record continuous data to support the long-term characterization study of the site whose first results were reported in Di Giovanni *et al.* (2021).

The first installation of the seismic stations dates back to 2019 March and, since then, all three have been continuously upgraded to improve data quality. For example, SOE0 was initially placed on surface in a shed next to a water pump with poor insulation and equipped with a Guralp 3ESPCD with poor mass alignment. At that time all three stations had an input range of 40 V/pp. In December 2019, SOE0 was moved to a dedicated vault 210 m southeast and the sensor was replaced with a Trillium 240. Also, the first underground station SOE1 was updated with a new sensor and digitizer in 2020 July. In particular, the digitizer was set to a high gain configuration by changing the input range from 40 to 4 V/pp. to optimize background noise studies. The other stations were kept at 40 V/pp. In 2021 June, SOE2 also had the input range set at 4 V/pp. The implications of SOE1 and SOE2 acquiring data at with different gain settings are shown in Figs 3(c)–(f), the main difference being the measured noise floor that is limited by detector noise between 3 and 7 Hz at SOE2. The details of the stations and their changes are reported in Table 1. All stations have a sampling frequency of 100 Hz except SOE1 which, from 2019 March until 2020 July, sampled at 40 Hz. Figs 3(a) and (b) also show the comparison of the spectra calculated over one week before and after the improvements of the year 2020 for SOE1. The new gain configuration marked an improvement between 3 Hz and 7 Hz where the observed noise is now close to Peterson's low noise model (Peterson 1993) as shown in Fig. 3(b), and not limited by detector noise as in Fig. 3(a).

The presence of two road bridges (Fig. 4), at ≃ 850 and ≃ 1300 m from the site respectively, made also necessary the temporary deployment of five Sunfull 4.5 Hz geophones, coupled to Innoseis Tremornet nodes (Beker *et al.* 2016), to characterize their contribution to the overall background seismic noise. Four of these geophones were deployed under the bridges, one per each pillar of each bridge. The fifth was deployed at the mine, near SOE0. These sensors were deployed for a period of five days between 2021 November 7–11. The seismic stations network is also complemented by a Davis Vantage Pro2 weather station installed outside the control room of the mine and providing data about wind speed and direction, rain, temperature and humidity. The sampling rate is set at 30 min.

4 SEASONAL NOISE VARIATIONS IN THE MICROSEISMIC BAND

To fully characterize the seismic noise at the site, a study of the effect of sea waves on the overall seismic background noise recorded at the site is necessary. In fact, the understanding of microseisms, their dependence on the season and their direction can potentially be exploited for the design of active seismic isolation systems.

As for any location on Earth, between 0.1 and 1 Hz the spectra from Sos Enattos (Di Giovanni *et al.* 2021) are dominated by the peak associated to background seismic noise from sea waves (Peterson 1993). This peak is related to the so called double-frequency microseisms (DFM) occurring at twice the frequency of sea waves and originating from nonlinear interactions of standing ocean waves causing a pressure wave to propagate toward the ocean floor (Longuet-Higgins 1950). A comprehensive discussion on the generating and propagation mechanisms of microseisms is beyond the scope of this paper and will not be covered here, but can be found in Longuet-Higgins (1950), Cessaro (1994) and Ardhuin *et al.* (2011, 2019).

For the specific case of Sos Enattos, Naticchioni *et al.* (2014) and Di Giovanni *et al.* (2021) have already conducted some preliminary analysis about the correlation of wind speed and atmospheric pressure variations with seismic noise and discussed the correlation between sea-wave height and seismic noise. In particular, it was found that between 0.1 and 1 Hz seismic noise in Sos Enattos is strongly correlated with sea-wave height from a portion of the Tyrrhenian sea between Sardinia and the Gulf of Lyon (Di Giovanni *et al.* 2021), a region that was already identified by Chevrot *et al.* (2006) as the main source of microseisms in the Mediterranean Sea. Nevertheless, at that time the available data did not cover a time span long enough to appreciate possible seasonal variations in the noise levels and their association with sea activity. Since we now have more than two years of almost continuous seismic data, it is possible to provide an in-depth study of how the noise level changes with respect to time and its relationship with sea-wave height. In particular, we focus on the two years from 2019 March until 2021 July to provide two full winter–summer cycles. Moreover, since Di Giovanni *et al.* (2021) showed that at the depth of the two underground seismic stations, the noise amplitude variation in the microseismic band is negligible with respect to the surface, we will focus on the underground seismic station SOE2 only.

Sea-waves data were downloaded from the open data service of the European Union called Copernicus Marine Environment Monitoring Service (CMEMS). CMEMS provides reference information on the dynamics of the ocean and marine ecosystems for the global ocean and the European regional seas. In particular we download information from the Mediterranean Sea Waves forecasting system (MEDSEA, Korres *et al.* 2019) and select a subregion of the Tyrrhenian Sea from 1° to 16.5° E and from 35° to 46° N. The MEDSEA data set consists of time-series of wave-height data sampled every hour (hourly mean) with a coordinates-grid resolution of

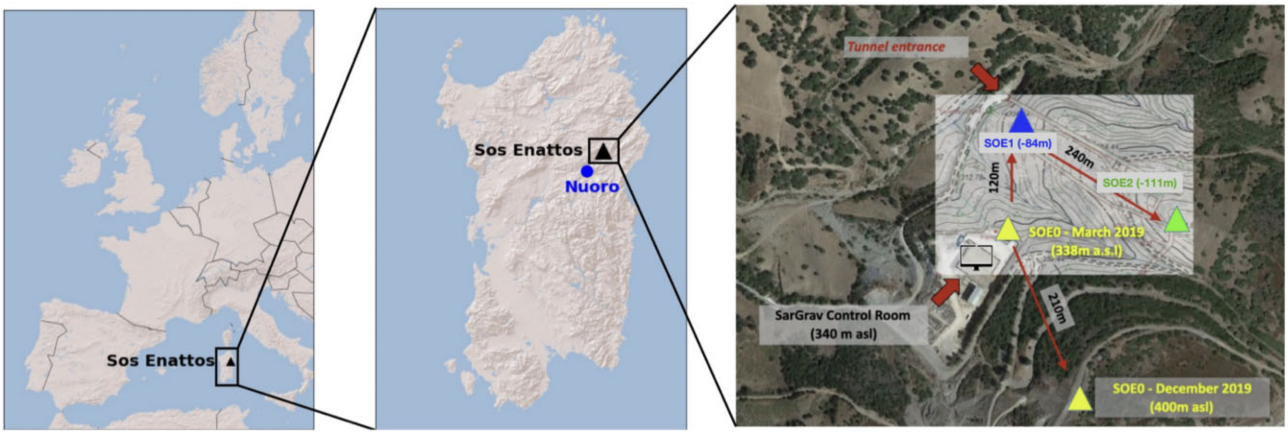

Figure 2. Left: location of Sardinia and Sos Enattos in Europe. Centre: location of Sos Enattos in Sardinia. The site is located 30 km NE of the city of Nuoro. Right: placement of the permanent seismic stations at the mine. The map shows the old and current installation of SOE0 (yellow) with SOE1 (blue) and SOE2 (green). Picture adapted from Di Giovanni *et al.* (2021).

4.6 km (Korres *et al.* 2019). To achieve this sampling and resolution, MEDSEA uses a model that interpolates all available satellite weather observations (Korres *et al.* 2019).

Fig. 5 summarizes the seasonal variation of seismic noise amplitude and shows a correlation between maximum microseismic noise levels and local autumn and winter. To estimate this variation, the spectra were calculated on 1 hr long segments with a 50 per cent overlap; then, from the distribution of the mean amplitudes of the segments between 0.1 and 1Hz calculated for every week, we inferred the weekly mean and the percentiles; outliers were removed according to periods with known data quality issues. Later, all remaining data points exceeding a certain threshold in σ were removed. Similarly, to calculate the peak stability, the weekly mean of the frequency of the microseismic peak was taken; outliers were removed as for the former procedure. Gaps in the data are related to periods in which SOE2 was offline for servicing.

Fig. 5 also shows that the lowest frequencies are excited during winter, when the sea is more rough than during summer (Figs 6 and 7, top panel). These figures are in agreement with previous studies focusing on the global climate imprint on microseisms (Aster *et al.* 2008; Stutzmann *et al.* 2009) and the relationship with the seasonality of sea waves activity is clear as outlined in Fig. 6, where sea activity reaches a maximum in winter and is minimal in summer. An example of how different conditions of the Mediterranean Sea affect the observed spectra is shown in Fig. 7. The first two rows show the comparison between rough and quiet nearby sea respectively, the bottom row shows the evidence of an oceanic storm that will be discussed in the upcoming section.

4.1 Atlantic sea storms

Every year, low atmospheric pressure areas in the Atlantic Ocean generate powerful extratropical cyclones which form as cyclonic windstorms. These low pressure areas are very common over the North Atlantic and they trigger cyclones off the coast of North America that travel across the North Atlantic Ocean passing north of Scotland to later die in the Norwegian Sea. Occasionally, these cyclones follow a path further south and therefore have a significant impact over North-Western Europe (Hewson & Neu 2015).

To determine if and how these storms affect the seismic background noise in Sos Enattos, we have to look for periods in which an Atlantic cyclone is coincident with a period of quiet Mediterranean sea, otherwise activity in nearby seas may hide any trace of oceanic storms. In particular, oceanic sea waves are expected to manifest with a distinct excitation frequency, different from the Mediterranean Sea, as microseismic generation at various source areas has distinct preferred excitation frequencies (Koper & Burlacu 2015). But, if the excitation frequency of the Atlantic Ocean is too close to that of the Mediterranean Sea, any search could be vain during periods of nearby rough seas.

To avoid this superposition, we consult the archived weather bulletins on Atlantic storms (UK Meteorological office 2021) and, at the same time examine the conditions of the Mediterranean Sea using MEDSEA data (Korres *et al.* 2019). We find that two storms, Storm Brendan (UK Meteorological office 2021), that swept from the coast of Newfoundland (CAN) to the Norwegian Sea from 2020 January 10–19, and Storm Dennis (UK Meteorological office 2021) that originated off the coast of Rhode Island (USA) and made landfall in Norway during the time period 2020 February 11–18, are coincident with a period of quietness in the Mediterranean Sea.

Analysis of the spectra and sea-wave height of the Mediterranean Sea reveal that, in the aforementioned periods, the nearby seas cannot excite the low frequencies as we observe (e.g. bottom row of Fig. 7). In particular (Fig. 8), after analysing CMEMS data for the Atlantic-European North-West shelf (Tonani & Ascione 2021) and for the Biscay bay (Aouf *et al.* 2020), we observe that around 0.2 Hz, the spectral evolution follows the sea-wave trend of the Mediterranean Sea: the low level of seismic noise is in agreement with the quiet sea. On the other hand, at lower frequencies, we observe that seismic noise follows another distinct trend that is well in agreement with the evolution of sea-wave height in the Atlantic Ocean. Correlation analysis confirms this impression, with the Mediterranean Sea that is anticorrelated (correlation <-0.1) with seismic noise below 0.13 Hz where correlation with the Atlantic Ocean reaches its maximum (correlation >0.6). Other than the aforementioned storms, no other clear evidence of oceanic storms was found in the data.

This suggests that, in the case of Sos Enattos, the Mediterranean Sea generates higher frequency signals, whereas the Atlantic Ocean is a source region for longer period secondary microseisms (Figs 7 and 8). A similar effect has also been discussed by Anthony *et al.* (2022), who identified similar areas of the United States where two distinct secondary microseismic peaks are associated to different ocean basins. Furthermore, the fact that nearby seas excite higher

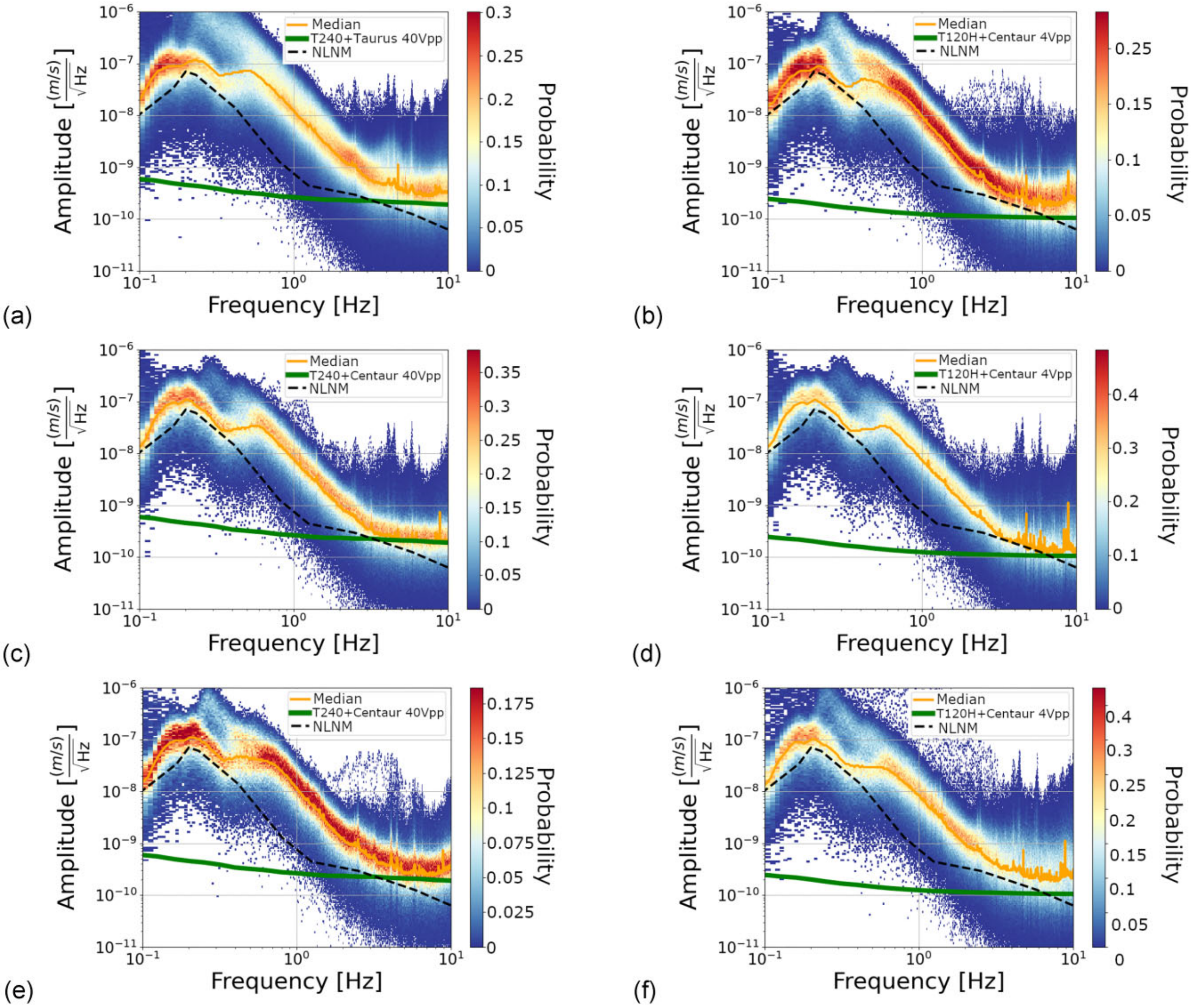

Figure 3. Probabilistic amplitude spectral densities for data quality improvements of SOE1 (a) before and (b) after the upgrades in 2020 July. (a) shows how, in the older configuration, we are limited by detector noise beyond 3 Hz, whereas, after the gain change in (b), we touch Peterson's low noise model between 3 and 7 Hz. The change in SOE1 meant that, between 2020 July and 2021 June when also SOE2 gain was set at 4 V/pp, the two underground stations acquired data with different gain settings, this led to a difference in the noise floors of the two detectors. (c) and (d) show the spectra calculated at night for one week at SOE2 and SOE1, respectively, highlighting the difference of the two noise floors (at night we expect to measure natural background noise only at all frequencies). (e) and (f) show the spectra calculated by day for one week at SOE2 and SOE1 respectively; in this case, with anthropogenic noise sources active during daytime, the difference in noise levels is very small and SOE2, set at 40 V/pp, is limited by detector noise only between 6 and 7 Hz. The spectra are calculated using the Welch's method with respect to velocity and in both cases we show the median of 128 s segments with a 50 per cent overlap over 7 d before and after the improvements. A comparison with Peterson's low noise model is also shown.

frequencies than far away oceans can be interpreted in the context of Koper & Burlacu (2015), who attributes the shorter-period peak to the local sea and the longer-period peak to more distant microseisms.

5 TRANSITIONAL NOISE

As outlined in the Introduction, the transition between microseismic noise and noise generated by anthropogenic activities happens between 0.5 Hz $< f <$ 1 Hz (Gutenberg 1958) and, on hard rock geology like in Sos Enattos, it can extend up to $f \simeq 5$ Hz (Seo 1997). Moreover, during strong oceanic activity, the impact of the noise in the microseismic band can be observed well into the anthropogenic frequency band. Similar high-frequency microseisms arising from water wave action at Great Lakes of mid-western United Stated have been studied in (Anthony *et al.* 2018). The effect is even more dominant at hard-rock and underground sites with low anthropogenic noise level (Seo 1997). One way of quantifying this effect is by comparing the temporal variation of the noise PSDs (Power Spectral Densities) in different frequency bands. Fig. 9(a) shows a spectrogram of the vertical component of the noise measured at the surface station SOE0 for a period of one week. Temporal variation of the noise for a particular frequency band is obtained by averaging the temporal variation of the noise PSDs across all frequency bins in that band. Fig. 9(b) shows the temporal variation of the noise

Table 1. Seismic stations. The depth of SOE1 and SOE2 is determined with respect to a standard reference point on top of the mine.

Station	Dates	Coordinates	Depth	Sensor	Digitizer	Sampling	Input range
SOE0	03/2019– 12/2019	40.444298 9.456815	–	Guralp 3ESPCD 120s	embedded embedded	100 Hz	40 V/pp
SOE0	12/2019– present	40.442520 9.457812	–	Nanometrics Trillium 240s	Nanometrics Taurus	100 Hz	40 V/pp
SOE1	03/2019– 07/2020	40.445509 9.456854	−84 m	Nanometrics Trillium 240s	Nanometrics Taurus	40 Hz	40 V/pp
SOE1	07/2020– present	40.445509 9.456854	−84 m	Nanometrics Trillium 120s Horizon	Nanometrics Centaur	100 Hz	4 V/pp
SOE2	03/2019– 06/2021	40.445457 9.456988	−111 m	Nanometrics Trillium 240s	Nanometrics Centaur	100 Hz	40 V/pp
SOE2	06/2021– present	40.445457 9.456988	−111 m	Nanometrics Trillium 360s	Nanometrics Centaur	100 Hz	4 V/pp

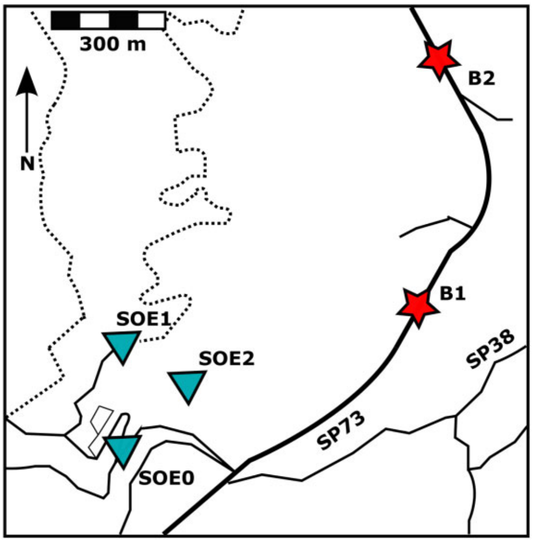

Figure 4. Map showing the location of the two road bridges, marked as B1 and B2, with respect to the three permanent seismic stations SOE0, SOE1 and SOE2. The solid lines represent concrete-roads at the site, and the dashed lines represent unpaved roads running along valleys.

PSDs in five different frequency bands. We observe that the frequency bands 0.1–0.5, 1–1.5 and 1.5–2.3 Hz follow a similar trend. Above 2.5 Hz the diurnal variation of the noise is dominant, which is due to the increased influence of the anthropogenic noise sources demonstrated by lower noise during weekends, as will be shown in Section 7.2.

Another way of determining the frequency up to which the oceanic noise impacts the noise spectrum is by computing the cross-correlation of the temporal variation of the noise PSDs between frequency bins. This results in a matrix of cross-correlations where the diagonal elements represent the auto-correlations and the off-diagonal elements represent the cross-correlations between different frequency bins. Fig. 10 shows the surface plot of the cross-correlation matrix estimated using the spectrogram shown in Fig. 9(a). A significant correlation is observed between the microseism band and the anthropogenic band up to frequencies of about 2 Hz. For simplicity we show the results corresponding to the vertical component of the seismic noise measured at the surface station. In principle, similar trends are observed for the horizontal components of the surface and the underground stations. This can be attributed to the long wavelengths of the seismic surface waves in the microseism band. These waves are almost unattenuated at shallow depths of about 100 m and have a significant impact on the anthropogenic noise band during increased oceanic activity. A similar analysis over other weeks of data reveal that the impact of the oceanic noise on the anthropogenic band can extend up to about 3 Hz when the microseism noise PSD is in excess of 10^{-10} $(\mathrm{m\,s^{-1}})^2\,\mathrm{Hz}^{-1}$.

6 WIND NOISE STUDIES

Although the seismic noise at $f > 1$ Hz is mainly anthropogenic, it was observed that strong wind and other atmospheric phenomena not only excite several frequencies in this frequency range, but are also among the main sources of noise in the transition from microseism to anthropogenic noise (Gutenberg 1958; Ward & Crawford 1966; Coward *et al.* 2005; Burtin *et al.* 2008; Smith & Tape 2019). In addition to that, wind can also manifest as broad-band noise up to $f \simeq 60$ Hz. For example, Withers *et al.* (1996) found that, in New Mexico, local wind speeds greater than 3 m s^{-1} generated significant seismic noise at higher frequencies (1–60 Hz), often completely overwhelming the otherwise coherent signals present in the background noise.

Wind can generate seismic noise locally by agitating structures such as trees, buildings or bridges, rattling windows or loose fixtures, slamming doors and can even directly couple with the ground (Johnson *et al.* 2019; Dybing *et al.* 2019). Wind driving tall structures to oscillate at a resonant frequency may generate comparatively lower frequency seismic waves, while wind slamming a door or window shut might generate a range of higher frequencies (Smith & Tape 2019). Here we investigate seismic noise in the frequency band 1–30 Hz that is generated by local wind, rather than in regional seas. To do this, we compare wind speeds and wind direction with the seismic data recorded at SOE0, SOE1 and SOE2. The wind-data (speed and direction) were recorded between 2020 June 12 and the end of 2021 March with a temporal resolution of 30 min.

6.1 Wind at Sos Enattos

The wind speed data (Fig. 12) have mean of 1 m s^{-1}. The wind speed and direction vary diurnally (Fig. 11), with strongest winds during the day and weakest in the evening and at night. Sos Enattos is located 25 km west of the nearest coast. Meso-scale sea/land breezes are generated in coastal areas as a result of the different heat capacities of the land and water. When the sunlit surface of the land increases in temperature more than the sea surface, the thermal contrast generates a pressure gradient between air over the land and sea (Miller *et al.* 2003). The result is a sea breeze

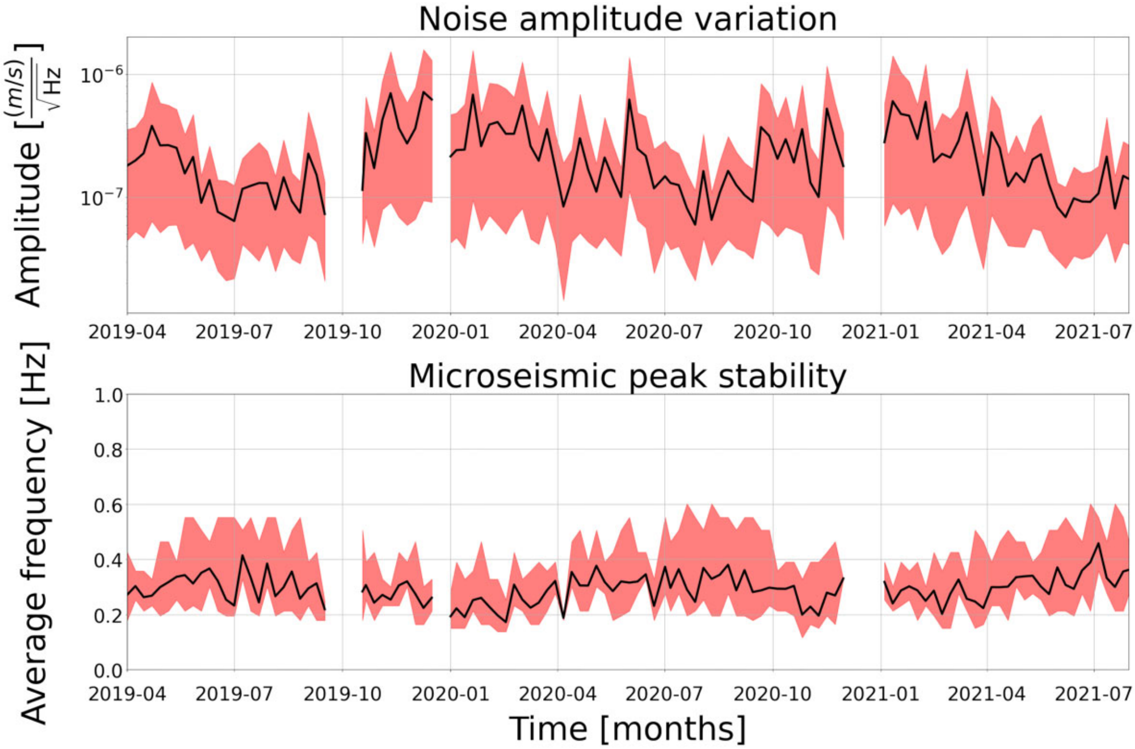

Figure 5. Top: seasonal noise amplitude variation calculated, after outlier removal, with a weekly mean of the average noise level between 0.1 and 1 Hz at SOE2 from 2019 April until 2021 June. Gaps in the plot are related to periods in which data were not available. The seasonality of the noise variation is apparent, reaching the maximum during winter and the minimum in summer. The red band includes the 10th and 90th percentile. Bottom: weekly mean of the microseismic peak characteristic frequency. Also in this case, a seasonality trend is apparent. Lower frequencies are privileged during winter whereas in summer the average frequency is as high as 0.37 Hz. The red band includes the 10th and 90th percentiles.

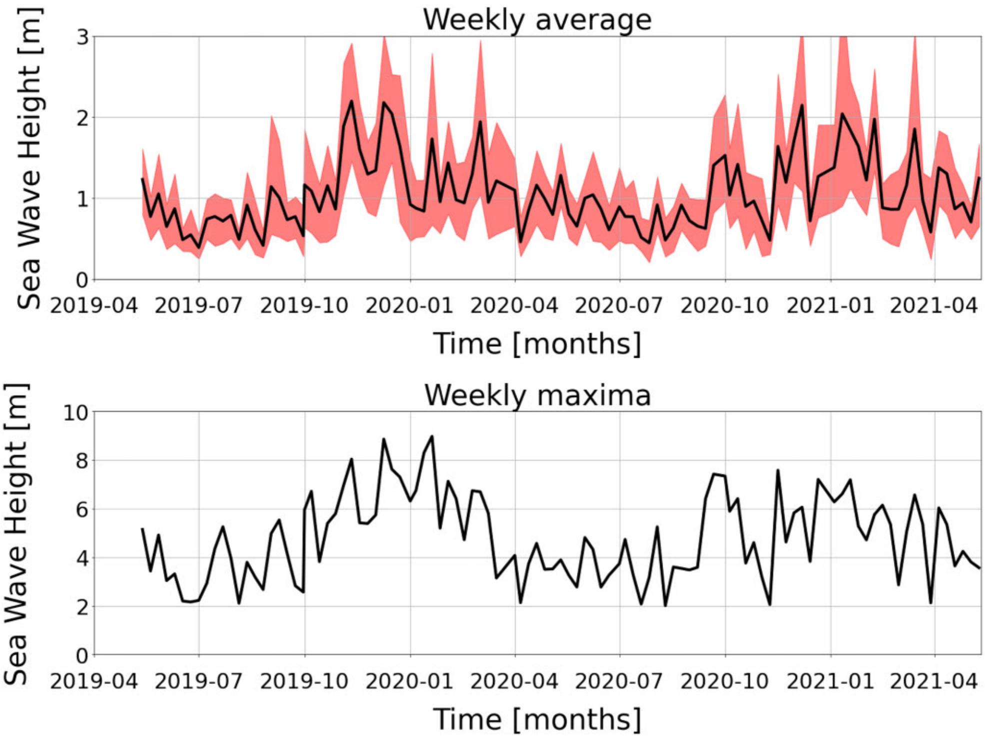

Figure 6. Top: weekly average sea-wave height data from MEDSEA (Korres *et al.* 2019) calculated all over the region from 1° to 16.5° E and from 35° to 46° N. The seasonality trend is in agreement with the seismic noise seasonality of Fig. 5. The red band includes the 10th and 90th percentiles. Bottom: weekly sea-wave height peak obtained all over the region from 1° to 16.5° E and from 35° to 46° N. Data from 2019 April are not available.

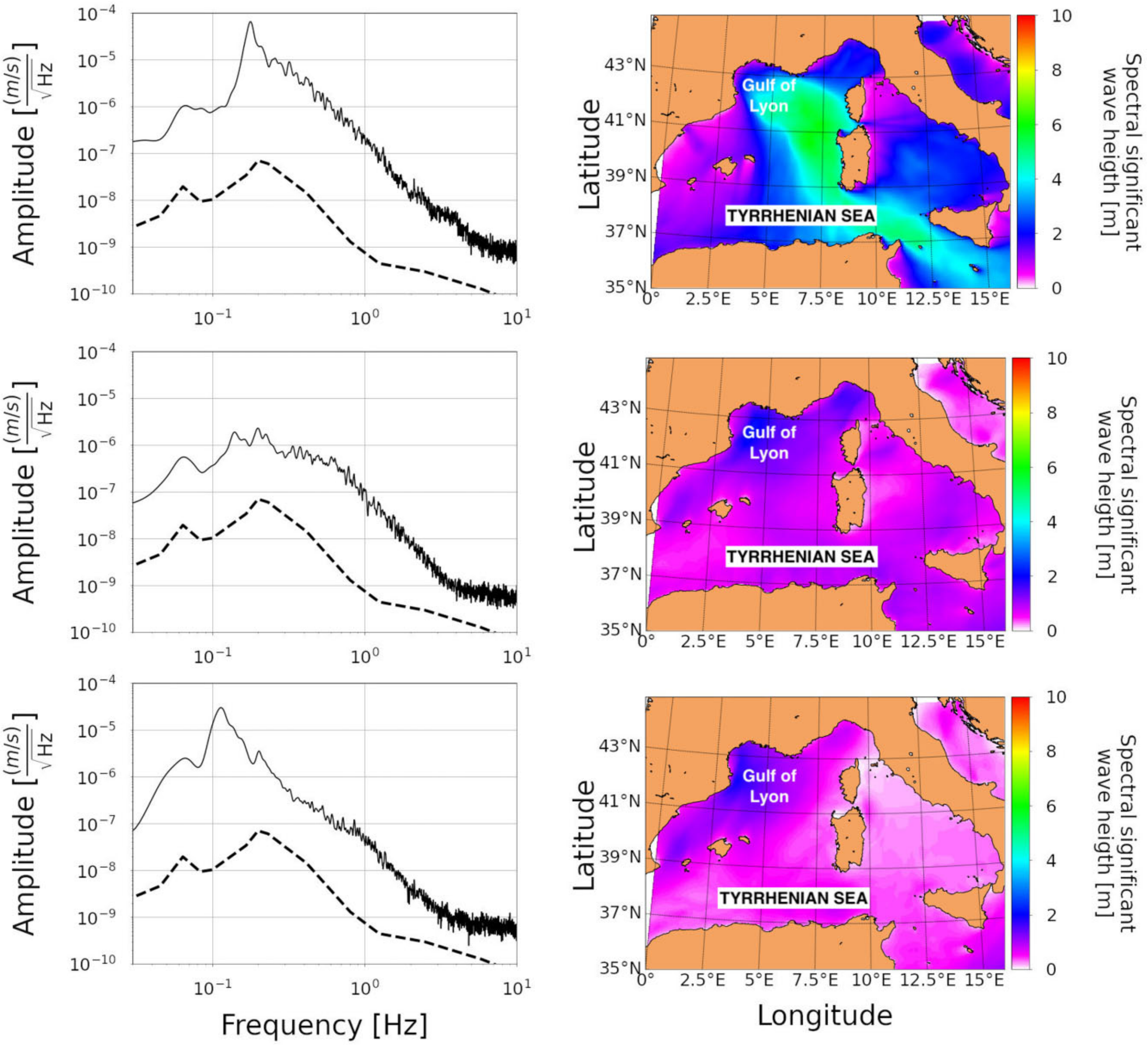

Figure 7. Comparison of SOE2 spectra against sea conditions in the Mediterranean Sea (Korres *et al.* 2019). The spectra are shown for the vertical component only and were calculated using the Welch's method over 1 hr of data. Sea-wave height data are obtained from CMEMS. Peterson (1993) new low noise model (NLNM) is also shown (dashed line). Top row: 2021-01-15T00:00—typical storms in the Mediterranean Sea, from the area identified by Chevrot *et al.* (2006) and Di Giovanni *et al.* (2021), manifest in the data as a peak centred between 0.17 and 0.22 Hz. Centre row: 2021-01-20T00:00—during calm periods, spectra are mainly flat and closer to the NLNM. Bottom row: 2020-02-17T00:00—evidence of an oceanic storm in the spectra. The conditions of the Mediterranean sea cannot cause the sharp peak observed at 0.12 Hz. Further analysis reveals the link with a storm in the Atlantic Ocean.

(sea to land) during the daytime and a land breeze (land to sea) during the night. The sea breezes tend to be oriented between 195°–45°, gentle land breezes winds at 90° and few winds at 100°–190° (0° is North).

There is observable seasonal variation in wind speed and direction at Sos Enattos. For instance, the nightly land breezes (90°) occur most strongly during Summer and in Autumn and least frequently and weakest in winter. This is likely a result of varied diurnal thermal contrast between land and sea across the seasons. The strongest winds tend to occur from the sea in spring while we observed no wind speeds above 4 m s^{-1} during Summer. The Mistral, a northwest wind, which blows from France may explain some of these stronger winds. The Mistral typically occurs in the winter and spring, and strongest in the transition between the two seasons.

6.2 Seismic noise and wind speed

To estimate the effect of wind on seismic noise, we calculate the spectra of seismic data following wind speed measurements acquired between 2020 June and 2021 March. The average wind speed across 2.5 s was sampled every 30 min. Minute-long seismic data segments following wind speed samples are tapered using a 60 s Hann window. The resulting spectra are sorted into bins based on the wind speed. Later, from the distribution of the spectra in every bin, we calculate the average and the percentiles shown in Fig. 13. The left-hand panel of Fig. 13 displays the spectra from SOE0 in the 1–30 Hz band. Elevated seismic energy occurs over a broad range of frequencies when higher wind speeds occur. The spectra from times when wind speeds exceed 4 m s^{-1} can have energy 2–3 orders of magnitude higher than when there is no wind. In particular

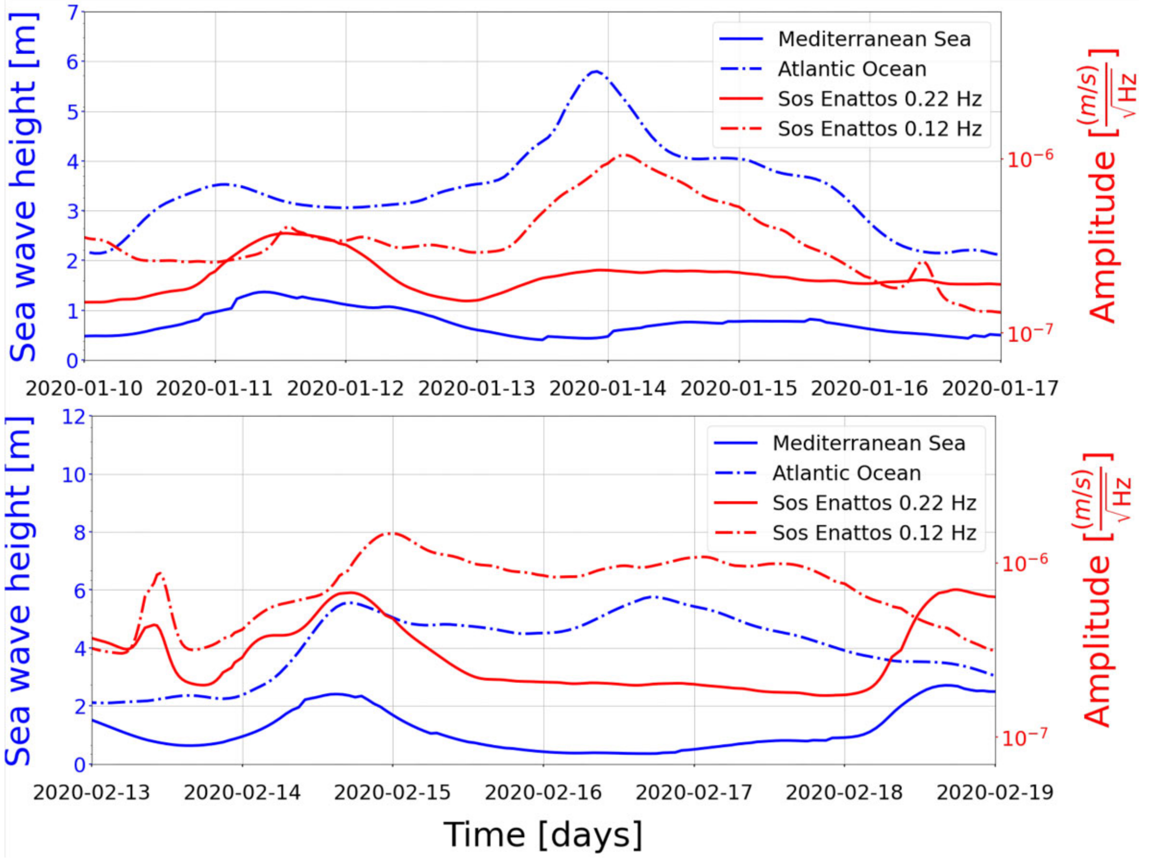

Figure 8. Top: spectral evolution of seismic noise at Sos Enattos (SOE2) at 0.22 and 0.12 Hz and evolution of sea-wave height during Storm Brendan (2020 January 10–19). Bottom: spectral evolution of seismic noise at Sos Enattos at 0.22 and 0.12 Hz and evolution of sea-wave height during Storm Dennis (2020 February 11–18). In both cases, the time-series of sea-wave height is obtained by averaging wave heights in the areas where correlation is maximized.

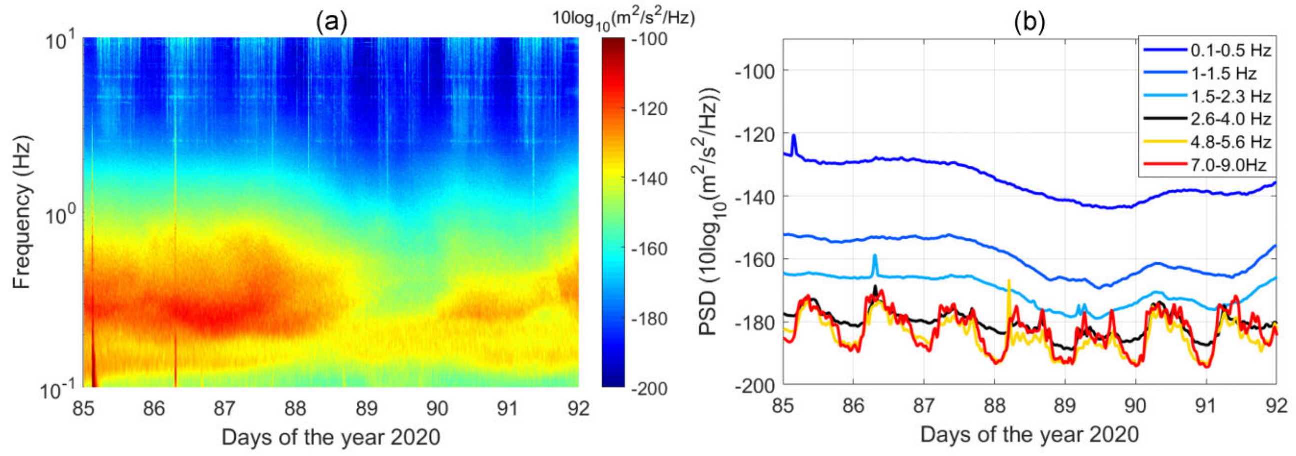

Figure 9. (a) Spectrogram of the vertical component of seismic velocity measured at the surface station SOE0 showing the evolution of microseism and anthropogenic noise over a period of one week. (b) Temporal variation of seismic noise averaged in six different frequency bands corresponding to the spectrogram shown in (a).

Fig. 13 shows strong seismic excitation on the surface in the frequency bands centred at 4.5, 9.2 and 11 Hz when wind speeds exceed 4 m s^{-1}. However, such an effect is not observed at the underground stations. The centre and right-hand panels of Fig. 13 show the spectra for SOE1 and SOE2 in the 1–30 Hz band. For times when there is no wind, the underground seismometers, SOE1 and SOE2, show a small reduction in background seismic noise compared to SOE0 at the surface. There is also a clear reduction in wind-generated seismic noise with depth in the frequency band considered. This is especially evident in the 1–6 Hz frequency band. At 111 m underground and frequencies above 6 Hz, the occurrence of wind results in only slightly elevated seismic energy with wind. We expect that this effect is the consequence of wind currents inside the tunnels of the mine. In fact, despite being underground, the tunnels have two

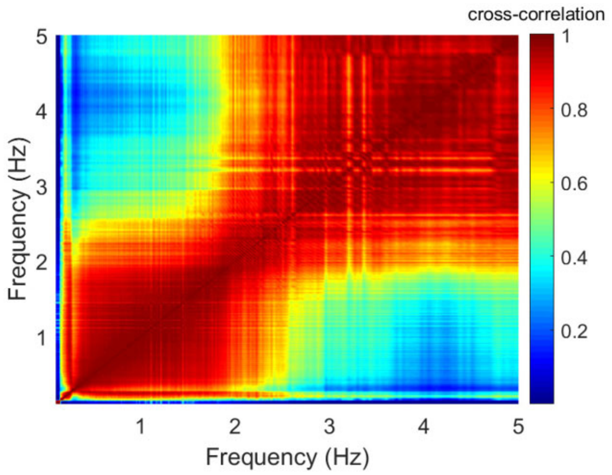

Figure 10. Frequency domain cross-correlation matrix (estimated from the spectrogram of Fig. 9) of the temporal variation of seismic noise showing significant correlation between the microseism noise and the anthropogenic band up to frequencies of about 2 Hz.

accesses (the main entrance and a shaft used for ventilation) that are open and therefore do not shield possible wind currents occurring with windy conditions outside. Planned future measurement campaigns with microphone arrays will allow for more thorough studies of the correlation between pressure variations inside the tunnels, wind and excess of seismic noise underground.

Moreover, despite stronger winds happening during day in coincidence with anthropogenic activities, the excess of seismic noise shown in Fig. 13 cannot be attributed only to anthropogenic noise. In fact, the evidence that, in Sos Enattos, anthropogenic noise is dominant from 2.5 Hz (Fig. 9), the presence of peaks whose intensity increases with wind speed on surface and the appearance of seismic excitation with wind also below 2.5 Hz suggest that the excess of seismic noise shown in Fig. 13 cannot be attributed to anthropogenic noise sources only.

7 VARIATIONS OF ANTHROPOGENIC NOISE

In this section, we focus on seismic signals of anthropogenic origin by analysing temporal variations that are linked to human activities. Seismic noise at the site exhibit a daily and weekly variation in power for frequencies greater than 2.5 Hz. Human activities are reduced during the night and on weekends, consequently an imprint of it can be observed on the measured noise level. In the frequency domain, the anthropogenic band is characterized by both broad-band and narrow-band noise. Broad-band noise can be generated from sources like vehicular traffic in nearby roads. Narrow-band noise typically originates from on-site machinery operating at a sharp frequency (Fiori *et al.* 2020b), nearby wind mills (Saccorotti *et al.* 2011; Marcillo & MacCarthy 2020) or even nearby road bridges (Koley *et al.* 2017).

Figs 14(a)–(c) show the most probable noise PSDs (mode of the distribution) measured on the surface and at the two underground stations corresponding to the EW, NS and the Z components, respectively. As expected, a major reduction in seismic noise is observed at the underground stations for frequencies greater than 2 Hz. These frequencies are characterized by several narrow-band peaks. The origin of these noise peaks is found in the presence of two road bridges nearby and is explained in Section 7.3. The least seismic noise up to frequencies of about 10 Hz is observed at the deepest stations SOE2. However for frequencies greater than 10 Hz, noise measured at SOE1 is about 3–4 dB less than SOE2. This is counterintuitive, since station SOE2 is located deeper than SOE1. A possible explanation is that station SOE1 is located in a more remote area and farther away from local roads (SP73 as shown in Fig. 4) at the site. Several narrow-band noise peaks centred at 8.33, 13.4 and 18.5 Hz are also observed (Figs 14a–c). As mentioned earlier, such peaks originate from machines operating near the seismometer installation. The diurnal and weekly variations in seismic noise is used to quantify the regularity of the noise wavefield at the site. The standard deviation of the estimated PSDs was used to measure the regularity of the noise. Moreover, the analysis is performed in several frequency bands which helps in quantifying the regularity of the noise as a function of frequency. A site with dominantly regular seismic wavefield is desirable for hosting ET. Quantifying the stationarity of the seismic noise does not only provide a general overview of the noise conditions, it also helps to prepare for future passive seismic campaigns to study the subsurface. For example, accurate extraction of the Green's function of the medium using seismic interferometry relies on an isotropic distribution of noise sources (Harmon *et al.* 2010). Furthermore we also use the PSDs of the noise to derive the temporal evolution of the peak-frequency and the signal-to-noise ratio (SNR) of all narrow-band noise peaks in the data. This enables us to understand the spatial and the temporal influence of these noise sources on the measured noise data. Overall these analysis serves as a reconnaissance study for future extensive and targeted seismometer array deployments at the site.

7.1 Data processing

To analyse the temporal variations of anthropogenic noise, we used data from the aforementioned seismic stations SOE0 (surface), SOE1(−84 m) and SOE2 (−111 m). In particular, we use the latest configurations of the seismic stations (Table 1) and, therefore, the analysis covers the time period from 2021 July 01 until December 31. Since in these 5 months there may be occasional gaps in the data, all days with more than 12 hr of data missing were discarded. Initially PSDs were generated for every day using a Hann window of length 128 s and an overlap of 16 s between consecutive windows. To further reduce the amount of data points, PSDs were averaged over 8 consecutive time windows. As a result the new time resolution of the PSDs was 848 s. Besides reducing the data points, averaging improved the SNR of the narrow-band noise peaks. This proved useful for tracking the peak frequency of the narrow-band noise. SNR was estimated as the ratio of the peak magnitude to the magnitude of the noise floor within a bandwidth of 0.5 Hz around the peak frequency. In order to generate weekly (7-d) variation of PSDs used in the analysis in Section 7.2, we concatenate the PSDs generated every 848 s over a period of 7 d. Next, the 7-d long modified periodograms were averaged along the frequency axis based on the frequency band of interest.

7.2 Temporal variation

Temporal variation of anthropogenic noise in different frequency bands can be used to estimate the day–night changes in the noise level during weekdays and weekends (Saturday and Sunday). Additionally, the standard deviation of the measured seismic noise can be used to decipher the regularity of the noise at the site corresponding to different frequency bands. Throughout this section, we

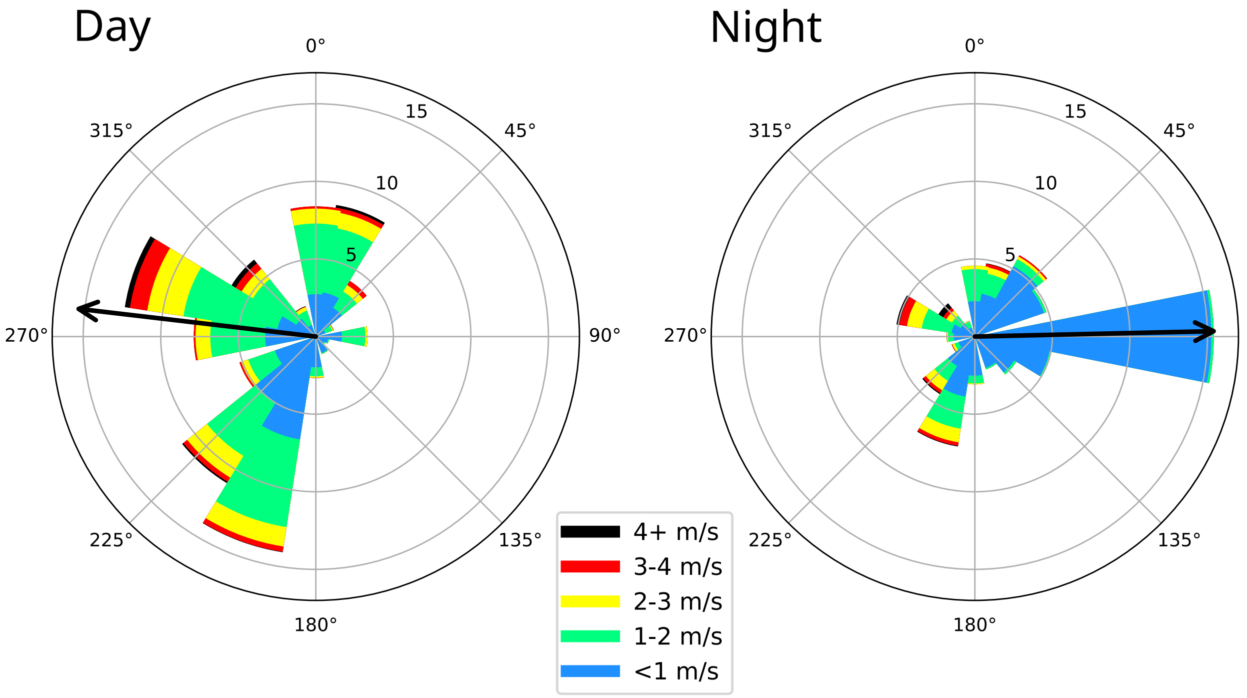

Figure 11. Wind rose diagrams for day (left) and night (right), showing the percentage of wind-speed measurements (radial axis) in different wind directions (azimuthal axis), and the proportion of different wind speeds (colour). The circular mean direction is shown with an arrow.

refer to daytime as the hours between 6 AM–4 PM UTC, and remaining hours in the day are defined as nighttime. Figs 15(a)–(c) show the most probable PSDs of the vertical component of the seismic noise corresponding to the day and night time, and estimated separately for the weekdays and weekends. In the frequency band 2–4 Hz, noise measured at the surface station is about 5 dBs (1 dB $= 10\log_{10}([(\mathrm{m\,s^{-1}})^2/\mathrm{Hz}])$) higher as compared to the noise measured underground. A day–night difference of about 6 dBs is observed during weekdays for both the surface and underground stations. On weekends, the day–night difference reduces to about 4 dBs, which is due to the reduction of seismic noise during the daytime on weekends. Figs 16(a)–(c) show the weekly variation in PSDs averaged across all bins in the band 2.6–4 Hz corresponding to the E-W, N-S and Z components, respectively. As stated in Sections 7.1, the temporal resolution of these variations is 848 s. All the three components of noise show a similar day–night and weekly variation. However, the overall noise level corresponding to the EW and the NS components at the underground stations is about 2–3 dBs lower as compared to the vertical component. A slight drop in the level of seismic noise is also observed at noon everyday which is due to the reduced anthropogenic activity at the site during lunch break.

In the frequency band 5–10 Hz an increase in the level of noise is observed for both the surface and the underground stations (Fig. 15). The minimum seismic noise floor is observed at SOE2. In this context, the seismic noise floor refers to the minimum PSD observed. Typically it corresponds to the seismic noise measured during night. The surface station shows an increase in diurnal variations from 5 dBs at 5 Hz to about 15 dBs at 10 Hz. The underground station SOE1 shows an increase in diurnal variation from about 5 dBs at 5 Hz to 10 dBs at 10 Hz. Since the underground station SOE2 is the quietest during night, the diurnal variation observed at SOE2 is about 15 dBs at 10 Hz. For frequencies greater than 10 Hz the maximum diurnal variation (15–20 dBs) is observed at the surface station on weekdays. The diurnal variation is reduced by about 3–4 dBs on weekends due to a reduction in the seismic noise measured during the daytime on weekends. A diurnal variation of about 8–10 dBs is observed for the underground station SOE1. For frequencies greater than 10 Hz, SOE1 becomes quieter during the daytime by about 4–5 dBs as compared to SOE2. The reason for this is that SOE1 is located farther away from nearby roads (road SP73 shown in Fig. 4) which is the one of the main sources of high-frequency noise at the site. However, the noise measured during the night at SOE1 and SOE2 are about the same. This is because the high-frequency sources of noise which impacts the daytime measurements are less active or absent at night. Figures showing the weekly variation of seismic noise in the frequency bands 4.8–5.6, 7–9, 9–11 and 13.6–17 Hz can be found in the Supporting Information to this article. The estimated diurnal variation for each of these frequency bands corresponding to the surface and underground stations are stated in Table 2. Corresponding to the statistics in Table 2, the day–night variation was first estimated for every day of data and the mean and standard deviations were then estimated using the 26 weeks of data as stated earlier.

Overall, studies of the temporal variation of the noise in the different frequency bands reveal that the diurnal variations increase with increasing frequency and that the noise measured during the day increases with increasing frequency. However, the seismic noise floor steadily decreases with increasing frequency (Fig. 15). From these observations, we could intuitively comment that the regularity of the seismic noise will decrease with increasing frequency and that the regularity of the seismic noise during the night will be higher than that during the day.

In order to establish the uniformity of the measured noise as a function of time and frequency, we check the regularity of the weekly noise pattern by calculating the rms variations (root mean square) of all PSDs from all the 26 weeks of data. The output is the weekly temporal evolution of the rms variation of the seismic noise. Similar to Figs 16(a)–(c), a day–night variation is observed.

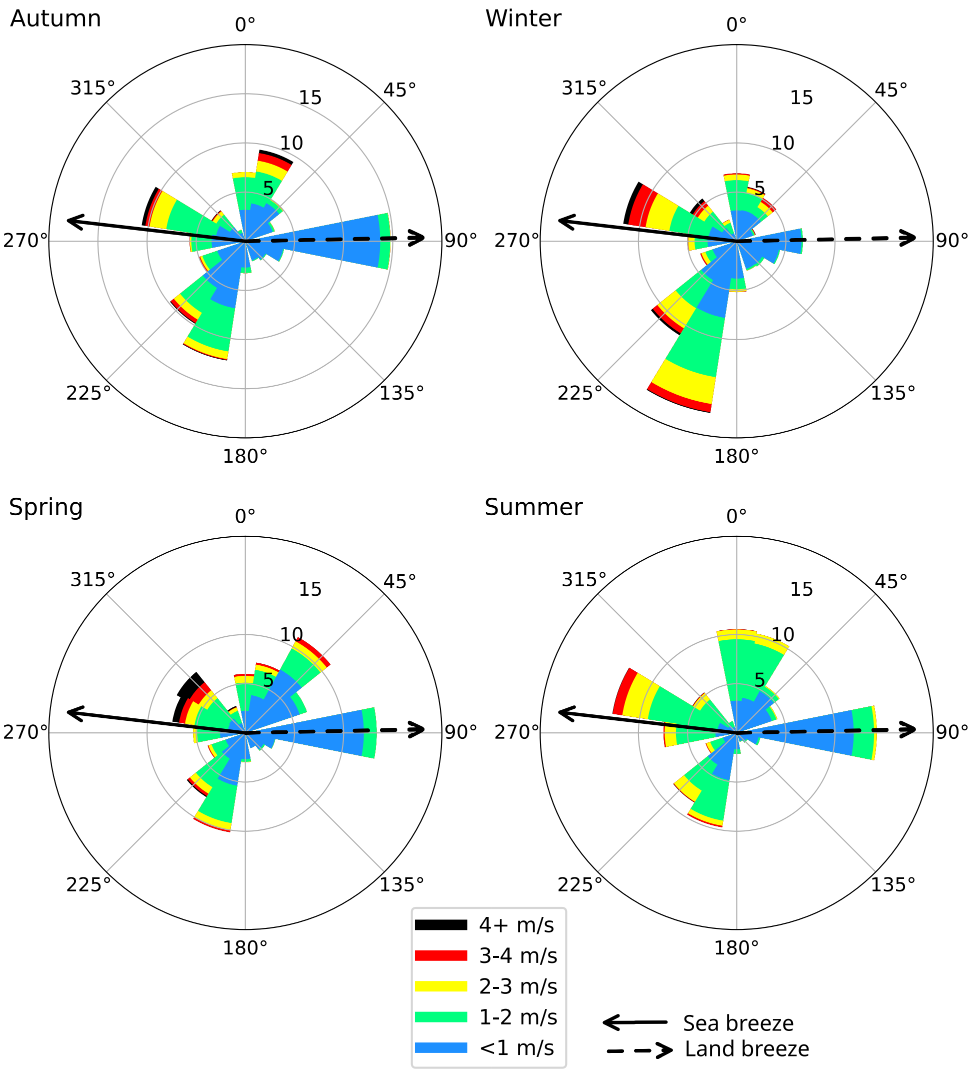

Figure 12. Wind rose diagrams for the four seasons, showing the percentage of wind-speed measurements (radial axis) in different wind directions (azimuthal axis from North), and the proportion of different wind speeds (colour). The sea and land breeze directions from Fig. 11 are displayed for comparison.

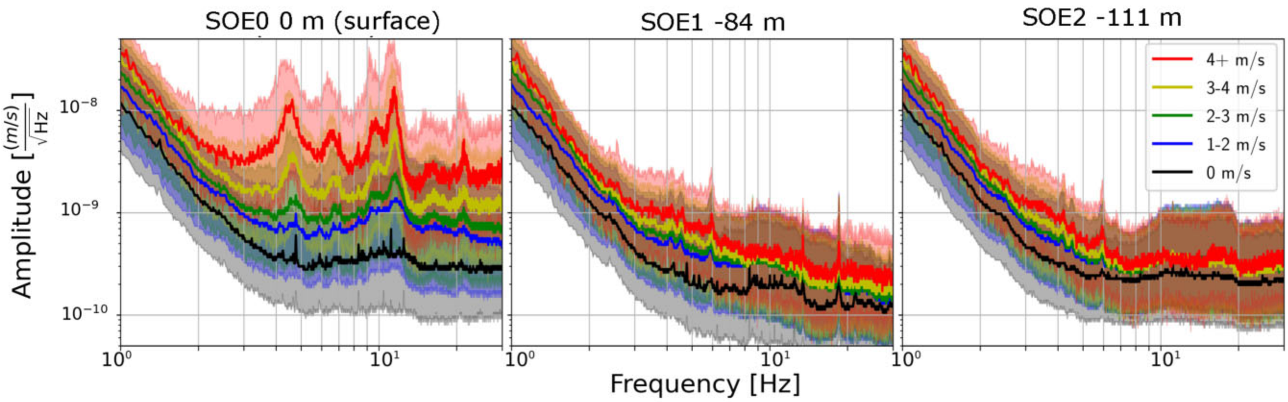

Figure 13. Probabilistic amplitude spectral density plots for SOE0 (left), SOE1 (centre) and SOE2 (right) computed over one minute long data segments starting at the wind speed measurement timestamp. The lines represent the 50th percentile and the shaded regions represent the space between the 10th and 90th percentiles. Each wind speed range is coded with a different colour. Noise floor in SOE2 is lower than SOE1 because, in the considered period, the input ranges of the two stations were different (see Section 3).

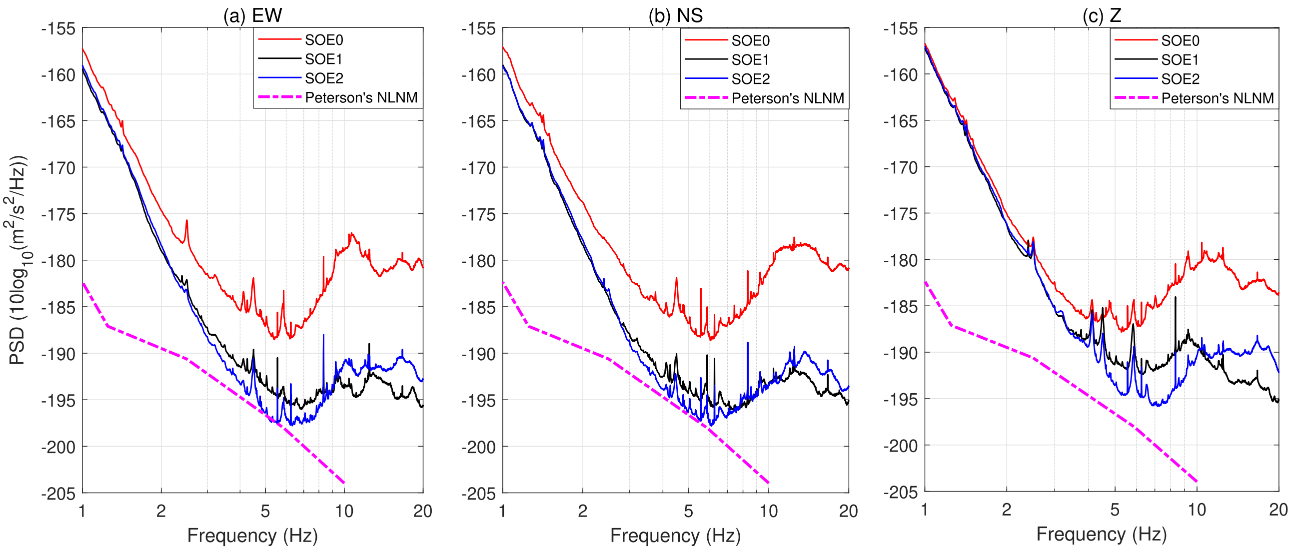

Figure 14. (a) Most probable PSD (mode of the distribution) corresponding to the EW component of the seismic noise data measured at SOE0, SOE1 and SOE2 and shown by the blue, red and the black curves, respectively. Peterson's new low noise model (NLNM) is shown with the dashed curve for comparison. (b) Same as (a), but corresponds to the NS component of the noise data. (c) Same as (a), but corresponds to the vertical component of the noise data. PSDs were computed using 128 s long Hann windows and an overlap of 16 s between consecutive windows.

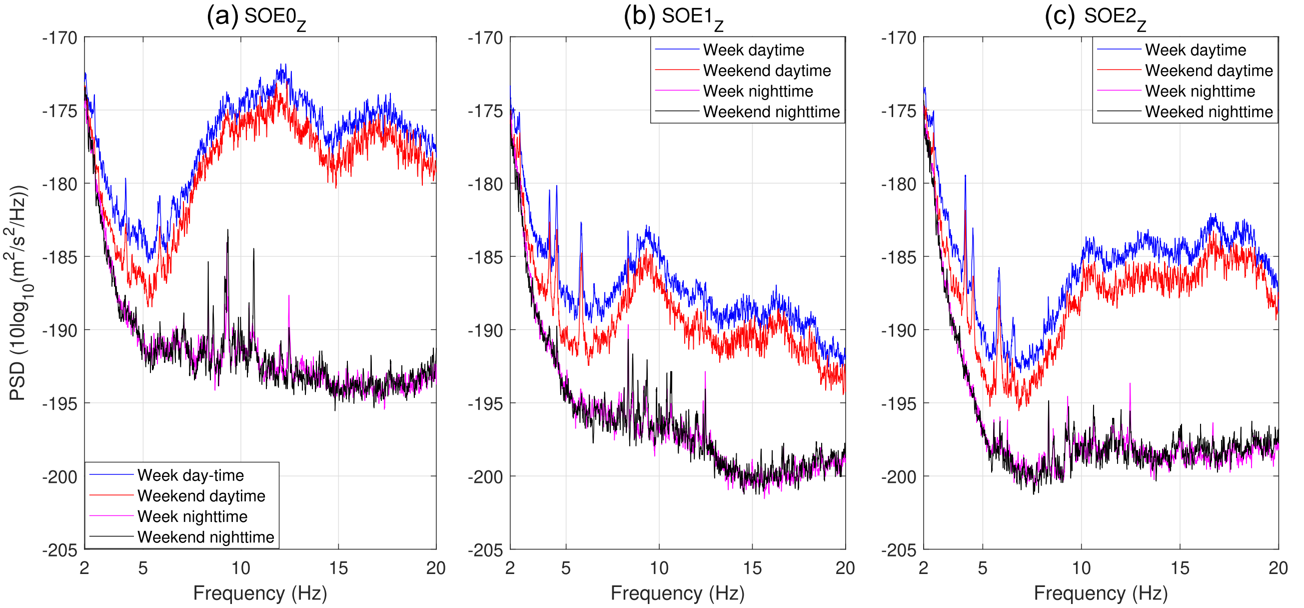

Figure 15. The blue and the red curves show the most probable PSDs of the vertical component of the seismic noise estimated during the daytime of weekdays and weekends, and the magenta and the black curves correspond to the PSDs estimated during the nighttime of weekdays and weekends for stations (a) SOE0, (b) SOE1 and (c) SOE2.

Figs 17(a)–(d) show the rms variation of the vertical component of the seismic noise PSDs as a function of day of the week in four different frequency bands of interest. The frequency band 2.6–3.95 Hz shows little diurnal variation in rms and implies that there is only a small change in regularity between day and night. This is what is expected, since the low-frequency noise tends to be dominated by far-away seismic sources and show little variation in strength between day and night. For higher frequencies, the rms during the day increases to about 8 dB for the surface station. The rms during the night is observed to be about 5 dB, implying that the noise measured at night is more regular than that measured during the day. The rms for the underground stations during the day is also slightly smaller than that observed for the surface station. This is because, the noise generated by local surface-sources impacts the underground seismic stations slightly less than it does to the surface station.

7.3 Bridge noise

Seismic noise measured at the surface and the underground stations at the Sos-Enattos mine comprises both broad-band noise and noise that appears as peaks in the noise spectrum. While some of these noise peaks exhibit a typical diurnal variation with a strong SNR, others appear as transients without any distinct temporal variation.

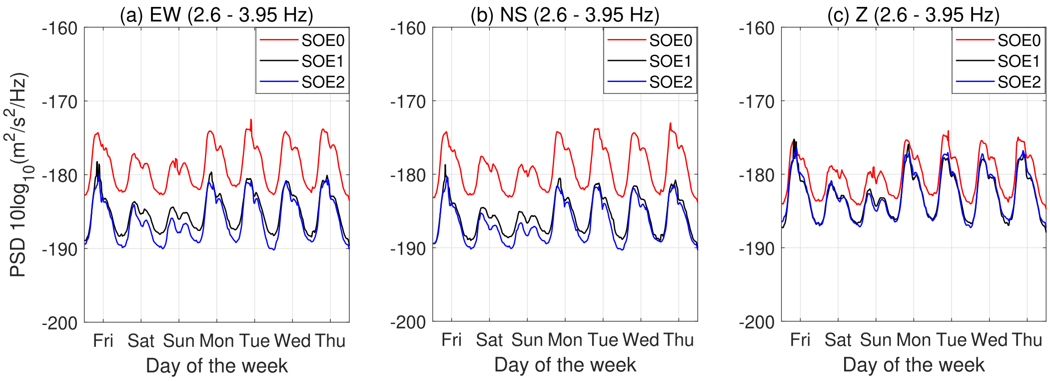

Figure 16. (a) The red, black and blue curves show the temporal variation of the PSDs averaged in the frequency band 2.6–3.95 Hz corresponding to EW component of the seismic noise measured at SOE0, SOE1 and SOE2. (b) and (c) are same as (a), but correspond to the NS and the vertical component, respectively.

Table 2. Mean diurnal variation of the noise PSD (1 dB = $10\log_{10}((\mathrm{m\,s^{-1}})^2\,\mathrm{Hz^{-1}})$) estimated for six different frequency bands corresponding to the seismic data measured at the surface (SOE0) and the underground stations (SOE1 and SOE2). Diurnal variation is estimated as the difference between the noise PSD measured around noon (10 AM–2 PM) and around midnight (9 PM–4 AM) every day.

Station name	Frequency bands (Hz)					
	2.6–4.0 Hz	4.8–5.6 Hz	7–9 Hz	9–11 Hz	11–13 Hz	13.6–17 Hz
SOE0-EW	5.9 ± 2.6	9.6 ± 3.7	13.5 ± 3.2	16.0 ± 4.2	16.0 ± 4.6	17.1 ± 3.5
SOE0-NS	6.1 ± 2.7	9.3 ± 3.7	11.6 ± 3.2	14.9 ± 3.9	17.1 ± 4.4	17.3 ± 3.5
SOE0-Z	5.9 ± 2.7	10.1 ± 4.4	13.4 ± 3.4	14.7 ± 4.5	16.1 ± 4.4	15.9 ± 3.5
SOE1-EW	5.3 ± 2.5	8.0 ± 3.2	9.8 ± 2.6	12.4 ± 3.1	13.2 ± 2.7	12.2 ± 2.5
SOE1-NS	5.2 ± 2.4	8.5 ± 3.1	9.4 ± 2.5	12.7 ± 2.8	13.3 ± 2.6	12.3 ± 2.6
SOE1-Z	6.3 ± 2.5	9.4 ± 3.35	11.7 ± 2.9	12.0 ± 3.0	9.4 ± 3.2	11.2 ± 2.8
SOE2-EW	5.8 ± 2.4	8.6 ± 3.4	7.9 ± 3.3	11.8 ± 2.8	12.6 ± 2.6	13.4 ± 2.4
SOE2-NS	5.3 ± 2.3	8.5 ± 3.4	8.3 ± 3.3	10.7 ± 2.5	12.8 ± 2.3	13.4 ± 2.3
SOE2-Z	6.4 ± 2.5	9.8 ± 3.4	11.2 ± 2.6	13.7 ± 3.2	13.9 ± 2.9	14.2 ± 2.8

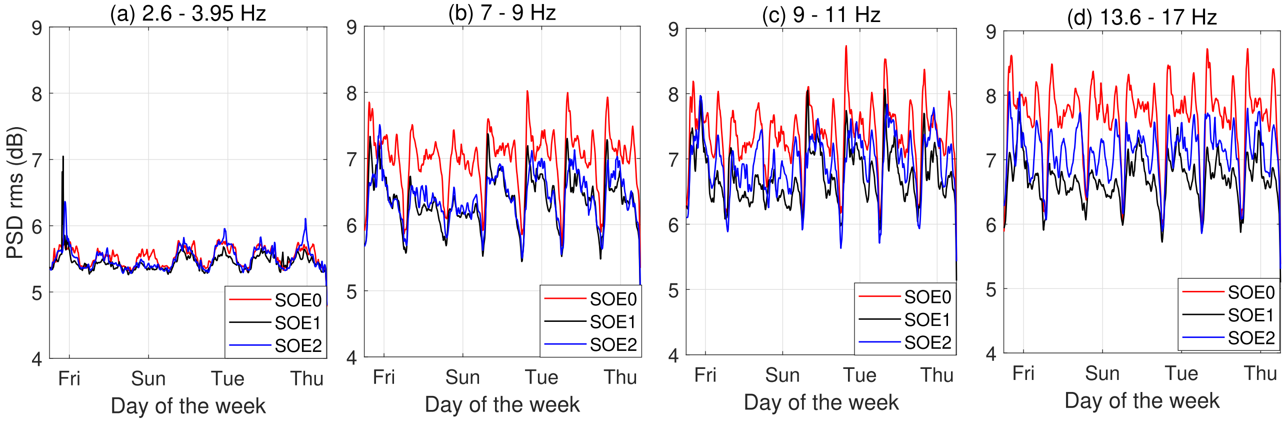

Figure 17. The red, black and blue curves show the temporal variation of the rms of the PSDs corresponding to the seismic noise measured at SOE0, SOE1 and SOE2 respectively for (a) frequency band 2.6–3.95 Hz. (b) Frequency band 7–9 Hz. (c) Frequency band 9–11 Hz. (d) Frequency band 13.6–17 Hz. All of the time-series refer to the vertical component of the seismometer.

Figs 18(a) and (b) show histogram plots of the PSDs measured at SOE0 during the daytime (6 AM–4 PM UTC) and the nighttime (4 PM–6 AM UTC), respectively. For better understanding, we show the PSDs in the frequency band 4–6 Hz. Broad peaks centred at 4.2, 4.5 and 5.9 Hz are observed during the day, and are absent during the night. Over shorter timescales typically spanning a day, these peaks show a day–night variation and are almost stationary with respect to the changes in peak frequency. However, on tracking the peak frequency over a year, we observed that these peaks show a drift in frequency. In order to track the temporal evolution of these peaks, we used an SNR threshold of 2.0 in the frequency domain. The drift is correlated with seasonal changes with a higher peak frequency observed during winter and the vice-versa during summer. Figs 19(a)–(c) show the drift in frequency of these noise peaks over a time period of about 500 d. It is worth noting that the rate at which each of these noise peaks drift in frequency is not the same. A linear relation is observed between the peak frequency of these noise peaks and the temperature measured at the site. Temperature

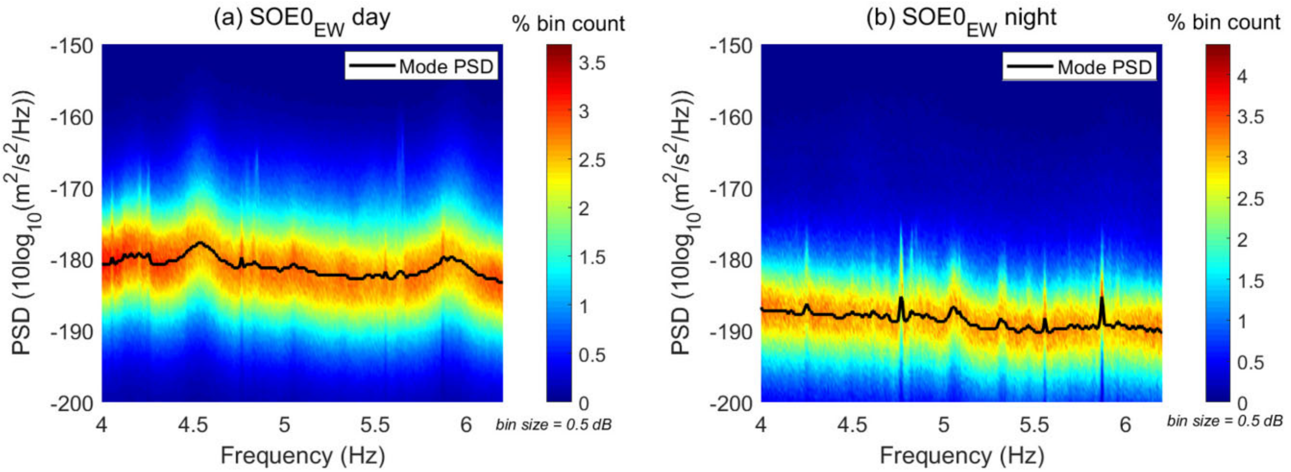

Figure 18. (a) Probability density functions of the seismic noise PSD measured at the surface station SOE0 estimated corresponding to the day-time data showing two broad peaks centred at 4.5 and 5.9 Hz. (b) Same as (a), but corresponds to the nighttime data. Mode of each of the distributions is shown with the black curve. The two broad spectral peaks observed in day are not observed during the night. Additionally several other narrow-band peaks are observed with a higher SNR during the night.

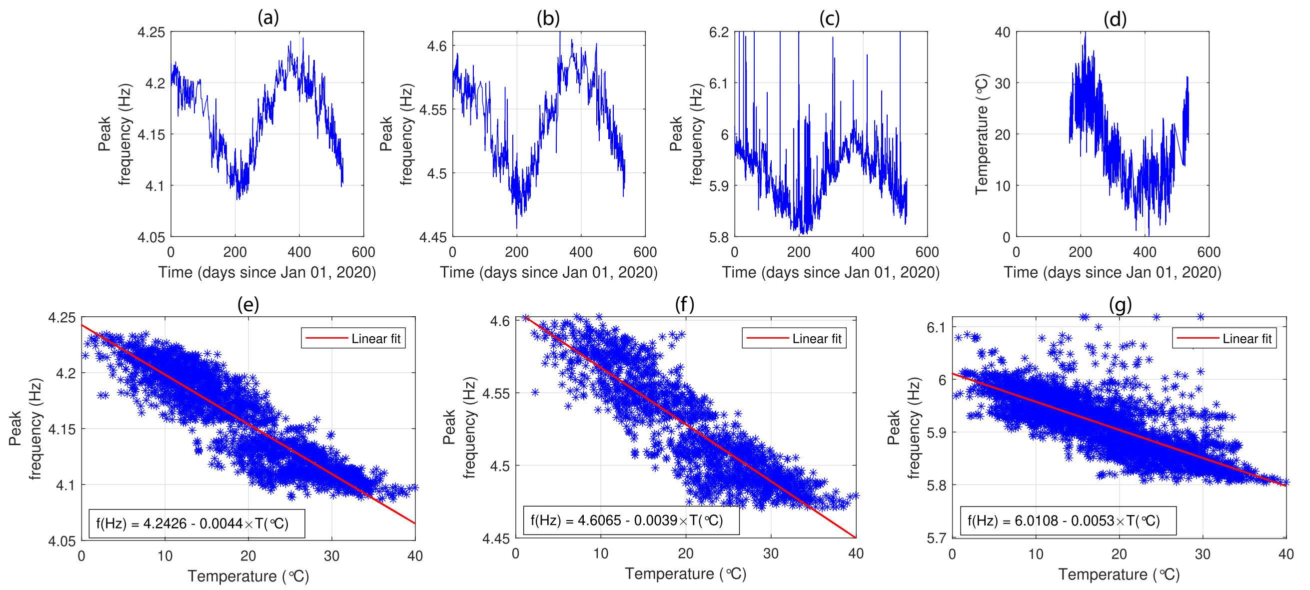

Figure 19. (a)–(c) show the drift in frequency of the 4.2, 4.5 and the 5.9 Hz noise peaks observed at SOE2, respectively. (d) Temperature variation measured at the site between 2020 June–2021 June. (e)–(g) show the scatter plots of the frequency of each of the three noise peaks versus the temperature variation observed at the site. A linear relation is observed which is shown using the red solid line.

at the site was acquired every 30 min between 2020 June–2021 June (Fig. 19d). In order to perform a correlation analysis between the two, timestamps for the peak frequency and the temperature data needed to be synchronized. Since the frequency of the noise peaks could not be identified at a regular interval owing to varying level of seismic noise at the site, an interpolation was performed to sample the peak-frequency variation at timestamps same as the acquired temperature data. Figs 19(e)–(g) show a scatter plot of the peak frequency versus the acquired temperature data at the site. The linear relation between these are also shown in the figures. This change in peak frequency is likely due to shrinkage and/or expansion of the structure of the bridges changing it properties as reported by Farrar *et al.* (1996), Zhou & Yi (2014), Gilbert (2017) and Cai *et al.* (2021). As the temperature increases, the resonant frequency of a bridge decreases, which is what we observe (the minimum frequency is reached during summer). Acquiring the engineering details of the construction of the bridges and the deployment of temperature sensors on the structure itself may allow, in the future, for a more detailed study of the correlation between temperature and resonant frequency variations, potentially also on a diurnal scale.

Besides the aforementioned peaks, there are several other peaks with smaller bandwidth that are distinctly visible during the nighttime. The higher seismic noise floor during the day obscures these peaks and they are visible in the spectrum with a much lower SNR. Tables showing a list of all the peaks that are observed in each of the three stations can be found in the Supporting Information to this paper. In this section, we discuss the origin of the broad noise peaks.

The surface station SOE0 exhibits broad noise peaks centred at frequencies of 2.55, 4.16, 4.55, 5.92, 6.7, 9.8, 11.5, 16.4, 18.75

Table 3. Distance of the three stations SOE0, SOE1 and SOE2 to each of the road bridges B1 and B2.

Station name	Distance to B1 (km)	Distance to B2 (km)
SOE0	1.00	1.54
SOE1	0.90	1.29
SOE2	0.74	1.25

and 19 Hz. While most of these peaks are observed in all the three components, peaks centred at 16.4 and 19 Hz are observed only in the Z and the N-S component of the noise data. Additionally, a peak centred at 18.75 Hz is observed in the E-W component. However, this peak is not observed in the other two components of the data. Previous studies at the AdVirgo site (Acernese *et al.* 2004; Koley *et al.* 2017) have shown that such peaks in the seismic noise data can originate from road bridges located within a few kilometres of the measurement location.

The Sos Enattos mine is bordered in the North by two road bridges located on the *Strada Provinciale 73 (SP73)*. Fig. 4 shows the location of the three stations and the two road bridges which are marked as B1 and B2. The distance of each of the road bridges to the three stations are stated in Table 3. Vertical component geophones with resonance frequency of 4.5 Hz were positioned beneath the two bridges for a period of five days between 2021 November 07 and 11. Data were continuously acquired at a sampling rate of 250 Hz. Seismic data acquired beneath the bridges were then cross-correlated with the seismic data acquired at the three stations SOE0, SOE1 and SOE2. The normalized cross-spectrum $C_{XY}(f)$ at frequency f between stations X and Y over M data segments is

$$C_{XY}(f) = \left| \frac{\sum_{n=1}^{n=M} X_n(f) Y_n^*(f)}{\sqrt{\sum_{n=1}^{n=M} X_n(f) X_n^*(f) \sum_{n=1}^{n=M} Y_n(f) Y_n^*(f)}} \right|. \quad (1)$$

$X_n(f)$ and $Y_n(f)$ represent the Fourier transform of the nth segment of the seismic data acquired at stations X and Y respectively, '$*$' represents the complex conjugate operator and $|.|$ represents the absolute value of a complex number. The blue curves in Figs 20(a) and (b) show the PSDs of the seismic data corresponding to bridges B1 and B2, respectively. PSD of the seismic noise data acquired at SOE0 during the same time is shown with the red curve in Figs 20(a) and (b). Several of the peaks that are observed beneath the bridges are also observed at SOE0, however these peaks are attenuated by over two orders of magnitude when observed at the Sos Enattos site. Figs 20(c) and (d) show the absolute value of the normalized cross-spectrum between SOE0 and bridges B1 and B2, respectively. Five noise peaks originating at bridge B1, centred at 2.55, 4.16, 4.55, 5.92 and 6.7 Hz show a cross-correlation magnitude of 0.5 or higher. However, cross-correlation between SOE0 and bridge B2 is relatively weaker as compared to SOE0 and bridge B1. This implies that these noise peaks observed at SOE0 are dominantly due to bridge B1. Above 7 Hz, there is no significant correlation between the noise beneath the bridges and the surface station SOE0.

Similar cross-correlation analysis was also performed for the underground station SOE2. During the bridge noise measurements, underground station SOE1 was not operational, hence a similar cross-correlation analysis could not be performed. The blue and the red curves in Fig. 21(a) show the PSDs of the seismic noise measured beneath bridge B1 and at station SOE2, respectively. Similar to SOE0, peaks in the normalized cross-spectrum are observed at frequencies of 2.55, 4.16, 4.55, 5.92 and 6.7 Hz. However, correlation magnitudes between SOE2 and bridge B1 is stronger than that between SOE0 and B1. This is because, SOE2 is located underground and the impact of the local surface noise sources on SOE2 is less as compared to SOE0. A figure demonstrating the higher SNR of these noise peaks at SOE1 and SOE2 when compared to the SOE0 is available as Supporting Information to this paper. Similar to the observations for SOE0, SOE2 shows a weaker correlation with bridge B2 compared to bridge B1. Additionally, correlation magnitudes of about 0.4 were observed for a few peaks above 10 Hz. This was not observed in the correlation analysis for surface station SOE0. Fig. 21(b) shows the PSD of the seismic noise measured at SOE2 in the frequency band 10–20 Hz. Broad peaks centred at 10.5, 11.5, 12.6, 16.6 and 18.75 Hz are observed. Out of these peaks, significant correlations with bridge B1 are observed for the peaks at 10.5, 11.5 and 18.75 Hz. These peaks in the correlation are shown in Fig. 21(d).

7.4 High-frequency transients

In the previous section we discussed on the origin of some of the broad spectral peaks observed in the spectrograms of the seismic data. Besides these peaks, there are several other peaks in the data that appear as sharp spectral peaks and are transient in nature, implying that their statistical properties vary significantly with time. While most of these noise peaks are observed for a small percentage of the measurement time, some of these peaks are more stationary than others. Besides being observed with a high SNR in the spectrogram, these noise peaks are also observed for about 40–50 per cent of the measurement time. These peaks are the ones at 8.33, 12.5, 16.67 and 18.5 Hz (Figs 22a and b). While the first three peaks are observed at all the three stations, the 18.5 Hz peak is only observed at SOE1 (Fig. 22b). Tables 1–3 which can be found as supplementary to this paper lists the SNR and percentage of observation time for each of these noise peaks corresponding to each of the stations. Fig. 22(a) shows the spectrogram of the vertical component of the noise measured at SOE1 for a time span of one day and zoomed-in the frequency band 7–10 Hz. The peak at 8.33 Hz is marked as 'A' in the figure and is present for the entire day in the data, and visible with higher SNR during the night. Other peaks which change in amplitude and jumps in frequency are marked as 'B'. In order to understand the origin of all of these noise sources, a dense seismic array study is needed, and is beyond the scope of this work. However, the noise peaks at 8.33, 12.5 and 16.67 Hz are somewhat generic. In the time domain, these appear as sinusoidal-type seismic waves originating from rotating machinery. As observed in previous studies by Kar *et al.* (2006), Coward *et al.* (2005) and Fiori *et al.* (2020b), these frequencies correspond to the rotation frequency of electric motors and cooling fans at the site. For example, a 12 pole engine has a rotation frequency of 8.33 Hz (500 rpm), an 8 pole motor has a rotation frequency of 12.5 Hz (750 rpm) and a 6 pole motor has a rotation frequency of 16.67 Hz (1000 rpm). In the future, we also aim to carry out a dedicated 'switch-off test' of these devices to verify the impact of these noise sources. At present, such studies could not be arranged due to logistic issues. Future array studies should also be aimed at understanding the wave-type and the polarization of the noise originating from these noise sources.

8 CONCLUSIONS

We have presented a study of temporal variations of the seismic field at the Sardinia candidate site for hosting ET. Important for ET is to know the source distributions in terms of direction and

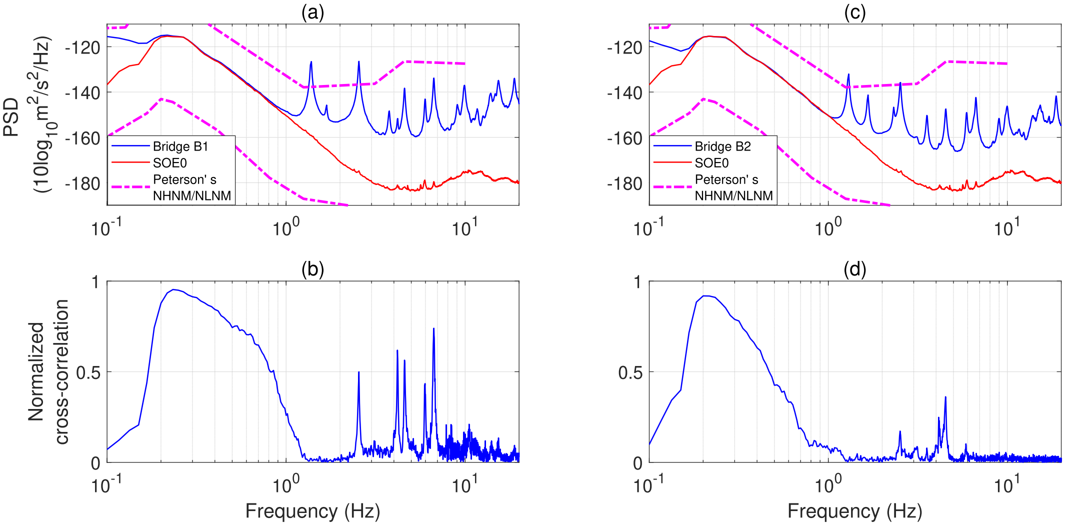

Figure 20. (a) The blue and red curves show the PSD of the vertical component of the seismic noise measured beneath bridge B1 and at station SOE0, respectively. (b) Normalized cross-spectrum between SOE0 and bridge B1. Several peaks show a strong correlation with the peaks originating at bridge B1. (c) Same as (a), but the blue curve corresponds to bridge B2. (d) Normalized cross-spectrum between SOE0 and bridge B2.

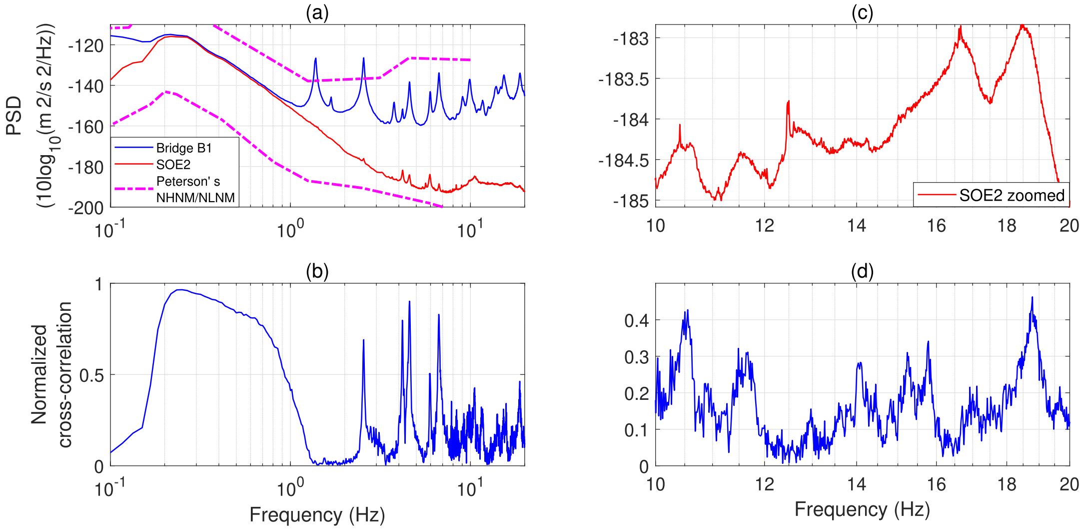

Figure 21. (a) The blue and red curves show the PSD of the vertical component of the seismic noise measured beneath bridge B1 and at station SOE2, respectively. (b) Normalized cross-spectrum between SOE2 and bridge B1. Several peaks show a strong correlation with the peaks originating at bridge B1. (c) PSD of the seismic noise measured at SOE2, zoomed in the frequency band 10–20 Hz. Several peaks centred at 10.5, 11.5, 12.5, 16.6 and 18.75 Hz are observed. (d) Normalized cross-spectrum between SOE2 and bridge B1 zoomed in the frequency band 10–20 Hz. Significant correlation is observed for the seismic noise peaks at 10.5, 11.5 and 18.75 Hz.

distance and how they vary with time. Since ET is proposed as an underground facility, one also needs to investigate the differences between temporal variations at the surface and underground. Understanding these factors will allow us to protect the site quality, and to potentially exploit recurring patterns in the seismic field for detector seismic isolation and control. What we found in our analysis is that the source locations of oceanic microseisms have a distribution characteristic for the seasons. Anthropogenic sources of seismic waves were identified out to distances of about 1.5 km (road bridges). This provides a first indication of the radius of the region around the ET vertices where human activities should be reduced. Seismic spectra measured underground at Sos Enattos show significant temporal variations in the NN band including diurnal and weekly cycles. For NN cancellation, we conclude that the filters might have to be adaptive or updated regularly to follow these variations.

We found that, between 0.1 and 3 Hz, seismic spectra are dominated by oceanic microseisms, generally produced by sea waves in the Mediterranean Sea, but occasionally also in the North Atlantic during strong storms. Peak amplitude of the seismic spectrum between 0.1 and 1 Hz varies by about a factor 10 over the year with highest amplitudes around $10^{-6}\,\frac{\mathrm{m}}{\mathrm{s}}\,\frac{1}{\sqrt{\mathrm{Hz}}}$ in the winter and lowest amplitudes during the summer. These variations are correlated with average sea-wave heights. At the ET candidate site, seismic waves forming the oceanic microseisms propagate mostly along the WWN-EES direction with likely origin in the Gulf of Lyon.

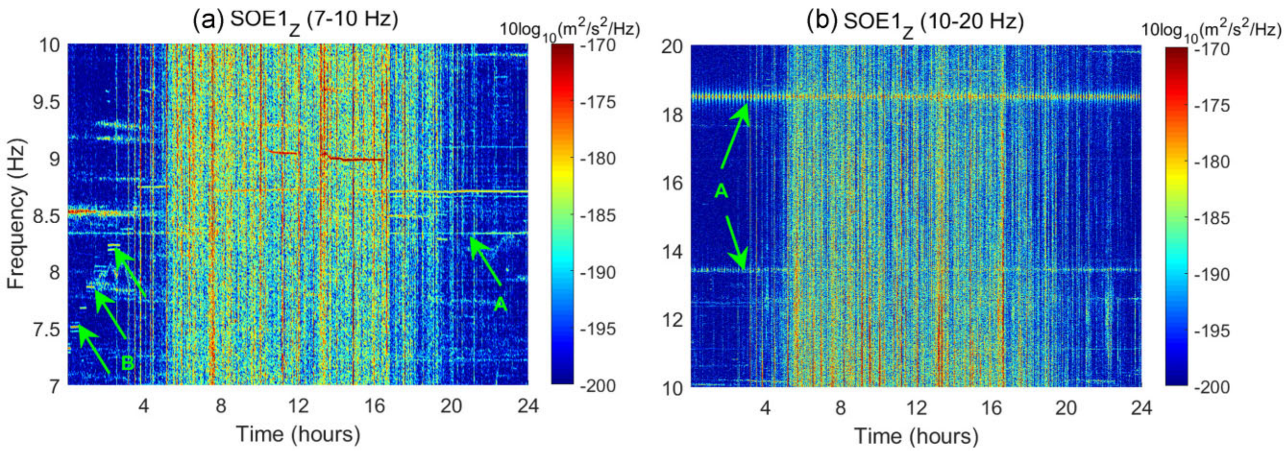

Figure 22. (a) Spectrogram of the vertical component of seismic noise observed at station SOE1 for a period of a day and zoomed-in the frequency band 7–10 Hz. (b) Same as (a), but corresponds to the frequency band 10–20 Hz. Two of the persistent noise peaks at 8.33 and 18.5 Hz originating from electrical motors at the site are labelled as 'A' in the figures. Other noise peaks that exhibit jumps in peak frequency and amplitude are labelled as 'B'.

Strong winds are a local source of seismic noise observable above 3 Hz. At the surface, the seismic-noise amplitude can increase by up to a factor 100. At the same time, we observed a strong attenuation of the wind-generated noise with depth. Already at 86 m depth, the impact of wind on seismic spectra is minor, that is, noise amplitudes increase by up to a factor 3 during strong wind. At 111 m depth, locally produced wind noise is negligible and excess noise only appears below 5 Hz connected to oceanic microseisms. This means that local wind noise will not pose a challenge to seismic isolation for ET, which will be at a depth of about 250 m, but it needs to be analysed whether gravitational fluctuations from surface vibrations can be an issue for ET during times of strong winds.

Our study also revealed anthropogenic contributions to seismic spectra. An easy way to identify it is through diurnal variations of seismic spectra connected to human activity cycles. These variations are visible also at 111 m depth; albeit with reduced strength. We characterized the contribution of specific anthropogenic sources: road bridges at about 1.2–1.5 km distance to Sos Enattos, and stationary motors. The contribution from the bridges is connected to the excitation of structural resonances of the bridges whose frequencies depend linearly on the temperature measured at the site. Measurements carried out at the base of the bridges were strongly correlated with measurements at Sos Enattos around some of the resonance frequencies. This calls out traffic as a potentially significant contribution to the otherwise low underground seismic noise. Motors at or near Sos Enattos are active during short periods and continuously. These are relatively easy to identify in the data, since they typically have characteristic rotation frequencies up-converted due to symmetries of the rotating parts. We can expect similar perturbations to be produced by pumps and ventilation systems in the future ET infrastructure, and it is advisable to develop mitigation techniques for this type of noise.

SUPPORTING INFORMATION

Supplementary data are available at *GJI* online.

Figure S1. (a) Correlation between seismic noise in Sos Enattos extracted at 0.12Hz and sea-wave height in the Atlantic Ocean during Storm Brendan. (b) Same as (a), but for Storm Dennis. (c) Correlation between seismic noise in Sos Enattos extracted at 0.12Hz and sea-wave height in the Mediterranean Sea during Storm Brendan. (d) Same as (c), but for Storm Dennis. The white area on the left in (a) and (b) is determined by the area coverage of the used data set (Tonani & Ascione 2021).

Figure S2. Rose histograms showing the microseism polarization for each trimester of 2020. The dominant direction points at the main microseism source region of the Mediterranean Sea.

Figure S3. (a) Average PSD of the Z component of the seismic noise data measured at SOE0, SOE1 and SOE2 shown by the blue, red and the black curves, respectively. Peterson's new low noise model (NLNM) is shown with the dashed curve for comparison. The noise peaks associated with the bridges near the site are observed at the underground stations SOE1 and SOE2 with a greater SNR as compared to the surface station SOE0. (b) A comparison of the cross-correlation between SOE0 and Bridge B1 (blue curve) and SOE2 and bridge B1 (red curve) is shown. A higher correlation is observed for the underground station SOE2.

Figure S4. (a) Spectral probability density function for SOE0; (b) spectral probability density function for SOE1; (c) spectral probability density function for SOE2. All three were calculated over 7 d from 2021-6-21T00:00 on 128s segments using the Welch's method. The green line represents the median of the PDF.

Figure S5. (a) The red, black and blue curves show the temporal variation of the PSDs averaged in the frequency band 4.8–5.6 Hz corresponding to seismic noise measured at SOE0, SOE1 and SOE2, respectively. (b)–(d) are same as (a), but correspond to the frequency bands 7–9, 9–11 and 13.6–17 Hz, respectively.

Table S1. Mean (μ) and standard deviation (σ) of the SNR of the peaks observed at SOE0 corresponding to each of the three components. The column ' time' states the percentage of the total observation time, when the peaks had an SNR greater than 2. '–' indicates that the noise peak was not observed. Noise peaks marked with a '$*$' correspond to the ones which originate due to the road bridges.

Table S2. Mean (μ) and standard deviation (σ) of the SNR of the peaks observed at SOE1 corresponding to each of the three components. The column ' time' states the percentage of the total observation time, when the peaks had an SNR greater than 2. '–' indicates that the noise peak was not observed. Noise peaks marked with a '$*$' correspond to the ones which originate due to the road bridges.

Table S3. Mean (μ) and standard deviation (σ) of the SNR of the peaks observed at SOE2 corresponding to each of the three components. The column ‘ time’ states the percentage of the total observation time, when the peaks had an SNR greater than 2. ‘–’ indicates that the noise peak was not observed. Noise peaks marked with a ‘$*$’ correspond to the ones which originate due to the road bridges.

ACKNOWLEDGMENTS

MDG gratefully acknowledges the support of the Italian Ministry of Education, University and Research within the PRIN 2017 Research Program Framework, no. 2017SYRTCN and INGV-Pisa for making their computational resources available. SK acknowledges the support through a collaboration agreement between Gran Sasso Science Institute and Nikhef and from the European Gravitational Observatory through a collaboration convention on Advanced Virgo +. JE would like to acknowledge the financial support of the International Research Agenda Programme AstroCeNT (MAB/2018/7) funded by the Foundation for Polish Science from the European Regional Development Fund and by the EU’s Horizon 2020 research and innovation program under grant agreement no. 952480 (DarkWave). MDG, SK and JE also acknowledge the use of the ETRepo computing cluster hosted by the Department of Physics of the University of Pisa (Italy).

This study was conducted within the framework agreement between Istituto Nazionale di Fisica Nucleare (INFN) and Istituto Nazionale di Geofisica e Vulcanologia (INGV). The authors would also like to express their gratitude to INFN that funded this project thanks to the Protocollo di Intesa tra Ministero dell’Istruzione, dell’Università e della Ricerca, la Regione Autonoma della Sardegna, l’Istituto Nazionale di Fisica Nucleare e l’Università degli Studi di Sassari finalizzato a sostenere la candidatura italiana a ospitare l’infrastruttura Einstein Telescope in Sardegna e al potenziamento di Virgo, and the University of Sassari that funded this project thanks to the Accordo di Programma tra la Regione Autonoma della Sardegna, l’Università degli Studi di Sassari, l’Istituto Nazionale di Fisica Nucleare, l’Istituto Nazionale di Geofisica e Vulcanologia, l’Università degli studi di Cagliari e l’IGEA S.p.a. finalizzato alla realizzazione nella Regione Autonoma della Sardegna di una infrastruttura a basso rumore sismico e antropico dedicata alla ricerca di base nell’ambito della rivelazione di onde gravitazionali, fisica della gravitazione, geofisica e sue applicazione (progetto SAR-GRAV). Intervento finanziato con risorse FSC 20142020 Patto per lo sviluppo della Regione Sardegna. The authors also acknowledge the Parco Geominerario Storico e Ambientale della Sardegna for its financial support. The authors’ grateful acknowledgment also goes to the contribution of the Fondi di Ateneo 2017 of Sapienza University of Rome and of the Fondi di Ateneo per la ricerca 2019 and Fondi di Ateneo per la ricerca 2020 of the University of Sassari.

DATA AVAILABILITY

The repository for the seismic noise data and meta data for stations SOE0 and SOE1 and the weather station is hosted by University of Pisa and can be made available upon request. The data from the station SOE2 are openly accessible through the FDSN service as INGV.IV.SENA, from 2019-10-18 until 2021-06-21, and as INGV.MN.SENA since 2021-06-21. The meta data can be downloaded from the INGV website. Sea-wave data are hosted by the EU open access service https://data.marine.copernicus.eu/productsCopernicus Marine Data Store. All the programs used in the data analysis can also be made available upon request.

REFERENCES

,Abdikamalov, E. *et al.* 2020. Gravitational waves from core–collapse supernovae, in *Handbook of Gravitational Wave Astronomy,* pp. 909–946, Springer Singapore, Singapore.

,Accadia, T. *et al.*, 2010. Noise from scattered light in virgo’s second science run data, *Class. Quantum Gravity,* **27**(19), 194011. doi: 10.1088/0264-9381/27/19/194011.

,Acernese, F. *et al.*, 2004. Properties of seismic noise at the virgo site, *Class. Quantum Gravity,* **21**(5), S433. doi: 10.1088/0264-9381/21/5/008.

F. *et al.*, 2014. Advanced virgo: a second-generation interferometric gravitational wave detector, *Class. Quantum Gravity,* **32**(2), 024001. doi: 10.1088/0264-9381/32/2/024001.

,Amann, F. *et al.*, 2020. Site-selection criteria for the einstein telescope, *Rev. Sci. Instrum.,* **91**(9), 094504 . doi:10.1063/5.0018414.

, R.E. *et al.*, 2018. The widespread influence of great lakes microseisms across the midwestern united states revealed by the 2014 polar vortex, *Geophys. Res. Lett.,* **45**(8), 3436–3444.

, R.E. *et al.*, 2022. Seismic background noise levels across the continental United States from usarray transportable array: the influence of geology and geography, *Bull. seism. Soc. Am.,* **112**(2), 646–668.

Aouf, , L. *et al.*, 2020. *Product User Manual for Atlantic-Iberian Biscay-Irish Wave Analysis and Forecast Product,* 31400 Toulouse, France.

, F. *et al.*, 2011. Ocean wave sources of seismic noise, *J. geophys. Res.,* **116,** C09004. doi: 10.1029/2011JC006952.

, F. *et al.*, 2019. Physics of ambient noise generation by ocean waves, in *Seismic Ambient Noise,* pp. 69–108, eds ,Nakata, N., et al. Cambridge University Press, Cambridge.

Aster,, R.C. *et al.*, 2008. Multidecadal climate-induced variability in microseisms, *Seismol. Res. Lett.,* **79,** 194–202.

M. *et al.*, 2021. Gravitational-wave physics and astronomy in the 2020s and 2030s, *Nat. Rev. Pys.,* **3,** 344–366.

Baiotti,, L. 2020. Binary neutron stars, in *Handbook of Gravitational Wave Astronomy,* pp. 495–526, Springer, Singapore.

Barausse,, E. & Lapi,, A., 2020. Massive black-hole mergers, in *Handbook of Gravitational Wave Astronomy,* pp. 851–884, Springer, Singapore.

Beccaria,, C. *et al.*, 1998. Relevance of newtonian seismic noise for the virgo interferometer sensitivity, *Class. Quantum Gravity,* **15**(11), 3339. doi: 10.1088/0264-9381/15/11/004.

Beker, M.G. *et al.*, 2012a. Newtonian noise and ambient ground motion for gravitational wave detectors, *J. Phys.: Conf. Ser.,* **363,** 012004. doi: 10.1088/1742-6596/363/1/012004.

MBeker,, .G. *et al.*, 2012b. Seismic attenuation technology for the advanced virgo gravitational wave detector, *Phys. Proc.,* **37,** 1389–1397.

MBeker,, .G. *et al.*, 2016. Innovations in seismic sensors driven by the search for gravitational waves, *Leading Edge,* **35**(7), 590–593.

Beker,, M.G., van den Brand,, J.F.J. & Rabeling,, D.S., 2015. Subterranean ground motion studies for the Einstein Telescope, *Class. Quantum Gravity,* **32**(2), 025002. doi: 10.1088/0264-9381/32/2/025002.

S. *et al.*, 2006. The nature of noise wavefield and its applications for site effects studies: a literature review, *Earth-Sci. Rev.,* **79**(3–4), 205–227.

Braccini,, S. *et al.*, 2000. The maraging-steel blades of the virgo super attenuator, *Meas. Sci. Technol.,* **11**(5), 467–476.

A. *et al.*, 2008. Spectral analysis of seismic noise induced by rivers: A new tool to monitor spatiotemporal changes in stream hydrodynamics, *J. geophys. Res.: Solid Earth,* **113**(B5), doi: 10.1029/2007JB005034.

Y. *et al.*, 2021. Influence of temperature on the natural vibration characteristics of simply supported reinforced concrete beam, *Sensors,* **21,** 4242. doi: 10.3390/s21124242.

Caprini,, C. & Figueroa,, D., 2020. Stochastic gravitational wave backgrounds of cosmological origin, in *Handbook of Gravitational Wave Astronomy,* pp. 1041–1094, Springer, Singapore.

L. *et al.*, 2004. The internal northern appennines, the northern tyrrhenian sea and the sardinia-corsica block, in *The Geology of Italy,* pp. 59–67, Italian Geological Society.

R.K., 1994. Sources of primary and secondary microseisms, *Bull. seism. Soc. Am.,* **84**(1), 142–148.

S. *et al.*, 2006. Source locations of secondary microseisms in western europe: evidence for both coastal and pelagic sources, *J. geophys. Res.,* **112**(B11), 301–320.

Coughlin,, M. *et al.*, 2017. Limiting the effects of earthquakes on gravitational-wave interferometers, *Class. Quantum Gravity,* **34**(4), 044004. doi: 10.1088/1361-6382/aa5a60.

D. *et al.*, 2005. Characterizing seismic noise in the 2–20 hz band at a gravitational wave observatory, *Rev. Sci. Instrum.,* **76**(4), 044501. doi: 10.1063/1.1876952.

M. *et al.*, 2021. A seismological study of the sos enattos area–the sardinia candidate site for the einstein telescope, *Seismol. Res. Lett.,* **92**(1), 352–364.

K.L. *et al.*, 2020. Terrestrial laser interferometers, in *Handbook of Gravitational Wave Astronomy,* pp. 37–84, Springer, Singapore.

S.N. *et al.*, 2019. Characteristics and Spatial Variability of Wind Noise on Near-Surface Broadband Seismometers, *Bull. seism. Soc. Am,* **109**(3), 1082–1098.

A. *et al.*, 2015. Environmental influences on the LIGO gravitational wave detectors during the 6th science run, *Class. Quantum Gravity,* **32**(3), 035017, d oi:10.1088/0264-9381/32/3/035017.

A., 1916. Näherungsweise integration der feldgleichungen der gravitation, *Sitzungsber. K. Preuss. Akad. Wiss.,* **1,** 688–696, doi: 10.34663/9783945561317-04.

ET Science Team, 2010. The einstein telescope: a third-generation gravitational wave observatory, *Class. Quantum Gravity,* **27**(19), 194002, doi: 10.1088/0264-9381/27/19/194002.

ET Science Team, 2011. *Einstein Gravitational Wave Telescope Conceptual Design Study,* III ET-0106A-10.

ET Science Team, 2020. *Design Report Update for the Einstein Telescope,* ET-0028A-20.

Eurostat, 2019. *Eurostat Regional Yearbook,* Publications Office of the European Union, Luxembourg.

C. *et al.*, 2014. Mantle dynamics in the mediterranean, *Rev. Geophys.,* **52,** 282–332.

C.R. *et al.* , 1996, United States, Variability of modal parameters measured on the Alamosa Canyon Bridge, https://www.osti.gov/biblio/432967

I. *et al.*, 2020a. Environmental noise in gravitational-wave interferometers, in *Handbook of Gravitational Wave Astronomy,* pp. 1–72, Springer, Singapore.

Fiori,, I. *et al.*, 2020b. The hunt for environmental noise in virgo during the third observing run, *Galaxies,* **8**(4), 82, doi: 10.3390/galaxies8040082.

R.L. *et al.*, 1961. Upper limit for interstellar millicycle gravitational radiation, *Nature,* **189**(4763), 473–473.

G.E., 1963. The nature of high-frequency earth noise spectra, *Geophysics,* **28**(4), 547–562.

G., 2017. *Statistical Models of I-15 Bridge C-846: Changes in Natural Frequencies due to Temperature, All Graduate Theses and Dissertations. 5260,* Utah State University.

B., 1958. Microseisms, in *Advances in Geophysics,* Vol. **5,** pp. 53–92, Elsevier.

N. *et al.*, 2010. Distribution of noise sources for seismic interferometry, *Geophys. J. Int.,* **183**(3), 1470–1484.

J., 2019. Terrestrial gravity fluctuations, *Living Rev. Relativ.,* **22**(6) , doi:10.1007/s41114-019-0022-2.

Harms,, J. *et al.*, 2022. A lower limit for Newtonian-noise models of the Einstein Telescope, *Eur. Phys. J. Plus,* **137**(6), 687 , doi:10.1140/epjp/s13360-022-02851-z.

B. & K., 2020. Isolated neutron stars, in *Handbook of Gravitational Wave Astronomy,* pp. 527–554, Springer, Singapore.

T.D. & U., 2015. Cyclones, windstorms and the imilast project, *Tellus A: Dynam. Meteorol. Oceanogr.,* **67**(1), 27128 , doi:10.3402/tellusa.v67.27128.

C.R. *et al.*, 2017. Broadband seismic noise attenuation versus depth at the albuquerque seismological laboratory, *Bull. seism. Soc. Am.,* **107**(3), 1402–1412.

INGV Seismological Data Center, 2006. Rete sismica nazionale (rsn), *Bull. Earthq. Eng.,* **13,** 35533596, doi: 10.13127/sd/x0fxnh7qfy.

C.W. *et al.*, 2019. Characteristics of ground motion generated by wind interaction with trees, structures, and other surface obstacles, *J. geophys. Res.— Solid Earth,* **124**(8), 8519–8539.

KAGRA Collaboration, 2019. Kagra: 2.5 generation interferometric gravitational wave detector, *Nat. Astron.,* **3,** 35–40.

C. *et al.*, 2006. Monitoring gear vibrations through motor current signature analysis and wavelet transform, *Mech. Syst. Signal Process.,* **20**(1), 158–187.

S. *et al.*, 2017. S-wave velocity model estimation using ambient seismic noise at virgo, italy, in *SEG Technical Program Expanded Abstracts 2017,* pp. 2946–2950, Society of Exploration Geophysicists.

Koley,, S., 2020. *Sensor networks to measure environmental noise at gravitational wave detector sites,* PhD thesis, Vrije Universiteit Amsterdam, Amsterdam.

Koley,, S., Bader,, M., van den Brand,, J., Campman,, X., Bulten,, H.J., Linde,, F. & Vink,, B., 2022. Surface and underground seismic characterization at terziet in limburg—the euregio meuse–rhine candidate site for einstein telescope, *Class. Quantum Gravity,* **39**(2), 025008, doi: 10.1088/1361-6382/ac2b08.

K.D. & R., 2015. The fine structure of double-frequency microseisms recorded by seismometers in north america, *J. geophys. Res.— Solid Earth,* **120**(3), 1677–1691.

G. et al., 2019. *Product User Manual for Mediterranean Sea Waves Analysis and Forecasting Product,* 1.3, CMEMS-MED-PUM-006-017.

LIGO and Virgo Collaboration, 2017a. Gw170817: observation of gravitational waves from a binary neutron star inspiral, *Phys. Rev. Lett.,* **119,** 161101 , doi:10.1103/PhysRevLett.119.161101.

LIGO and Virgo Collaboration, 2017b. Multi-messenger observations of a binary neutron star merger, *Astrophys. J.,* **848**(2), L12 , doi:10.3847/2041-8213/aa91c9.

LIGO and Virgo Collaboration, 2019. Gwtc-1: a gravitational-wave transient catalog of compact binary mergers observed by ligo and virgo during the first and second observing runs, *Phys. Rev. X,* **9,** 031040 , doi:10.1103/PhysRevX.9.031040.

LIGO Scientific Collaboration, 2015. Advanced ligo, *Class. Quant. Grav.,* **32,** 074001 , doi:10.1088/0264-9381/32/7/074001.

M.S., 1950. A theory of the origin of microseisms, *Phil. Trans. R. Soc. Lond.,* **243**(1), 35, doi: 10.1098/rsta.1950.0012.

LVK Collaboration, 2021a. Gwtc-2: compact binary coalescences observed by ligo and virgo during the first half of the third observing run, *Phys. Rev. X,* **11,** 021053 , doi:10.1103/PhysRevX.11.021053.

LVK Collaboration, 2021b. *Gwtc-3: Compact Binary Coalescences Observed by Ligo and Virgo during the Second Part of the Third Observing Run,* preprint, arXiv:2111.03606.

F. *et al.*, 2020. 3-d shear wave velocity model of the litosphere below the sardinia-corsica continental block based on rayleigh-wave phase velocities, *Geophys. J. Int.,* **220,** 2119–2130.

O.E. & J., 2020. Mapping seismic tonal noise in the contiguous united states, *Seismol. Res. Lett.,* **91**(3), 1707–1716.

Martynov,, D.V. *et al.*, 2016. Sensitivity of the Advanced LIGO detectors at the beginning of gravitational wave astronomy, *Phys. Rev. D,* **93,** 112004. doi:10.1103/PhysRevD.93.112004.

MedNet Project Partner Institutions, 1990. *Mediterranean Very Broadband Seismographic Network (Mednet)*. doi: 10.13127/SD/FBBBTDTD6Q.

S.T.K. *et al.*, 2003. Sea breeze: structure, forecasting, and impacts, *Rev. Geophys.,* **41**(3). doi:10.1029/2003RG000124.

Mukund,, N. *et al.* 2019a. Ground motion prediction at gravitational wave observatories using archival seismic data, *Class. Quantum Gravity,* **36**(8), 085005. doi:10.1088/1361-6382/ab0d2c.

Mukund,, N. *et al.*, 2019b. Effect of induced seismicity on advanced gravitational wave interferometers, *Class. Quantum Gravity,* **36**(10), 10LT01, doi:10.1088/1361-6382/ab1360.

L. *et al.*, 2014. Microseismic studies of an underground site for a new interferometric gravitational wave detector, *Class. Quantum Grav.,* **31**(105016), doi: 10.1088/0264-9381/31/10/105016.

L. *et al.*, 2018. Sargrav: the sardinia underground laboratory, a first module for the einstein telescope infrastructure, in *Proceedings of the 2018 Gravitational Wave Science & Technology Symposium,* https://agenda.infn.it/event/14869/contributions/26929/attachments/19271/21813/SARGRAVGRASS_LNat_v2.pdf

L. *et al.*, 2020. Characterization of the sos enattos site for the einstein telescope, *J. Phys.: Conf. Ser.,* **1468**(012242), doi: 10.1088/1742-6596/1468/1/012242.

J.R., 1993. *Observations and modeling of seismic background noise,* Tech. Rep. US Geological Survey.

D. *et al.*, 2020. Covid-19 lockdown and its latency in northern italy: Seismic evidence and socio-economic interpretation, *Sci. Rep.,* **10,** 16487, doi: 10.1038/s41598-020-73102-3.

P. *et al.*, 2020. The 2020 coronavirus lockdown and seismic monitoring of anthropic activities in northern italy, *Sci. Rep.,* **10,** 9404, doi: 10.1038/s41598-020-66368-0.

M. *et al.*, 2010. The einstein telescope: a third-generation gravitational wave observatory, *Class. Quantum Gravity,* **27**(19), 194002 , doi:10.1088/0264-9381/27/19/194002.

G. *et al.*, 2011. Seismic noise by wind farms: a case study from the virgo gravitational wave observatory, italy, *Bull. seism. Soc. Am.,* **101**(2), doi: 10.1785/0120100203.

P.R., 1984. Terrestrial gravitational noise on a gravitational wave antenna, *Phys. Rev. D,* **30**(4), 732–736.

B.F., 1989. Gravitational wave sources and their detectability, *Class. Quantum Gravity,* **6**(12), 1761–1780.

B.F., 1996. Gravitational-wave sources, *Class. Quantum Gravity,* **13**(11A), A219–A238.

K., 1997. Comparison of measured microtremors with damage distribution, in *JICA Research and Development Project on Earthquake Disaster Prevention,* pp. 306–320, Tokyo, Japan.

K. & C., 2019. Seismic noise in central alaska and influences from rivers, wind, and sedimentary basins, *J. geophys. Res.— Solid Earth,* **124**(11), 11678–11704.

E. *et al.*, 2009. Global climate imprint on seismic noise, *Geochem. Geophys. Geosys.,* **10**(11), doi: 10.1029/2009GC002619.

M. & I., 2021. *User Manual for Ocean Physical-wave Analysis and Forecast*. CMEMS-NWS-PUM-004-013_014

UK Meteorological office, 2021. *UK Storm Centre*. https://www.metoffice.gov.uk/weather/warnings-and-advice/uk-storm-centre/index

Virgo Collaboration, 2004. Properties of seismic noise at the virgo site, *Class. Quantum Gravity,* **21**(5), S433, doi: 10.1088/0264-9381/21/5/008.

Virgo Collaboration, 2006. Environmental noise studies at virgo, *J. Phys. Conf. Ser.,* **32**(1), 80, doi: 10.1088/1742-6596/32/1/013.

Virgo Collaboration, 2011a. *Characterization of the Virgo Seismic Environment,* preprint, arXiv:1108.1598.

Virgo Collaboration, 2011b. The seismic superattenuators of the virgo gravitational-wave interferometer, *J. Low Freq. Noise Vibr. Active Contr.,* **30,** 63–79.

Virgo Collaboration, 2014. Advanced virgo: a second-generation interferometric gravitational wave detector, *Class. Quantum Gravity,* **32**(2), 024001, doi:10.1088/0264-9381/32/2/024001.

Virgo Collaboration, 2022. The virgo o3 run and the impact of the environment, *Class. Quantum Gravity,* **39**(23), 235009, doi:10.1088/1361-6382/ac776a.

R.L. *et al.*, 2020. Research and development for third generation gravitational wave interferometers, in *Handbook of Gravitational Wave Astronomy,* pp. 37–84, Springer, Singapore.

H.S. & R., 1966. Wind-induced vibrations and building modes, *Bull. seism. Soc. Am.,* **56**(4), 793–813.

J., 1967. Gravitational radiation, *Phys. Rev. Lett.,* **18**(13), 498–501.

M.M. *et al.*, 1996. High-frequency analysis of seismic background noise as a function of wind speed and shallow depth, *Bull. seism. Soc. Am.,* **86**(5), 1507–1515.

G.D. & T.H., 2014. A summary review of correlations between temperatures and vibration properties of long-span bridges, *Math. Prob. Eng.,* **2014,** 19, doi: 10.1155/2014/638209.